THE ASTROPHYSICAL JOURNAL, 306:710–729, 1986 July 15

NUMERICAL STUDIES OF PARTICLE ACCELERATION AT TURBULENT, OBLIQUE SHOCKS WITH AN APPLICATION TO PROMPT ION ACCELERATION DURING SOLAR FLARES

ROBERT B. DECKER AND LOUKAS VLAHOS
Johns Hopkins University, Applied Physics Laboratory
Received 1985 November 11; accepted 1986 January 10

ABSTRACT

In this paper we address the problem of charged particle acceleration at oblique, fast-mode collisionless MHD shock waves when magnetic turbulence exists in the regions upstream and downstream of the shock. Specifically, we consider how the acceleration rate depends upon the angle θ_1 between the shock normal and the mean upstream magnetic field. To handle the general situation where θ_1, the turbulence level, the shock strength, and the energy of injected particles can assume a range of values, we perform fully relativistic, test particle simulations that involve integrating along particle phase space orbits in the shock turbulence system. As an application of the numerical code, we study proton acceleration at shocks under conditions appropriate to the lower solar corona to simulate prompt ion acceleration during solar flares. Particles undergo shock acceleration through a combination of the shock drift and first-order Fermi processes. For protons injected at 100 keV and left in the system for 500 gyroperiods ($\sim$7 ms in a 50 G magnetic field) we obtain the following results: (1) the percentage of protons accelerated above 10 MeV within 7 ms increases with increasing θ_1, from 0% at $\theta_1 = 0°$ to a maximum of 9% at $\theta_1 = 60°$; (2) the case $\theta_1 = 75°$ produces the largest, most rapid energy gains, with $\sim$1% of the protons accelerated above 50 MeV; (3) for $45° \lesssim \theta_1 \lesssim 75°$, a separate proton population with energies between 100 keV and 10 MeV is produced during a superfast acceleration phase lasting only $\sim$10 gyroperiods ($\sim$100 μs) after injection; (4) we compare the peak energy reached at $\theta_1 = 0°$ and energy spectrum produced at $\theta_1 = 75°$ with predictions from theoretical models, and find reasonable agreement, although discrepancies do exist. We discuss the implications of the numerical results as they pertain to time constraints and collisional loss processes during shock acceleration in the solar corona.

Subject headings: hydromagnetics — particle acceleration — shock waves — Sun: flares — turbulence

I. INTRODUCTION

The acceleration of ions and electrons by fast-mode, collisionless MHD shocks has been the topic of vigorous research activity over the past several years. Recent progress has been summarized and reviewed by Toptyghin (1980), Axford (1981), Drury (1983), Armstrong, Pesses, and Decker (1985), and Forman and Webb (1985). Shocks exist, or are strongly suspected to exist, in a variety of settings that span at least 14 decades of scale size and associated particle (ion) energies, ranging from $\sim 10^{10}$ cm and $\sim 10^5$ eV at the Earth's bow shock (e.g., Gosling *et al.* 1979; Lee 1982), to $\sim 10^{24}$ cm and $\sim 10^{19}$ eV at the galactic wind termination shock (Jokipii and Morfill 1985). Shock-accelerated ions have been observed in association with corotating shocks (e.g., Christon 1982) and solar transient shocks in the inner (e.g., Van Nes *et al.* 1984) and outer (e.g., Pyle *et al.* 1984) heliosphere. Some models have relied upon shocks to accelerate ions and electrons to high energies during solar flares (e.g., Acterberg and Norman 1980; Lee and Fisk 1982; Ellison and Ramaty 1985; Decker and Vlahos 1985*b*). Several years after the initial work by Axford, Leer, and Skadron (1978), Krymskii (1977), Bell (1978), and Blandford and Ostriker (1978), shocks bounding supernova remnants remain the most attractive means of accelerating galactic cosmic rays, at least to energies $\sim 10^{14}$ eV (Legage and Cesarsky 1983).

There are three known mechanisms that will accelerate charged particles to high energies (we refer to these as "energetic particles") at fast-mode shocks:

1. The shock drift mechanism (or more simply, drift mechanism) accelerates a particle as the particle's nearly helical orbit intersects the shock discontinuity several times during the process of reflection or transmission at a shock encounter (e.g., see review by Armstrong, Pesses, and Decker 1985). This mechanism is most effective when the angle θ_1 between the upstream magnetic field and the shock normal satisfies $45° \lesssim \theta_1 \leq 90°$ (i.e., the shock is quasi-perpendicular or perpendicular [$\theta_1 = 90°$]), which is the range within which both the convection electric field $\boldsymbol{\epsilon} = \boldsymbol{U} \times \boldsymbol{B}/c$ (which is proportional to $\sin \theta_1$ and parallel to the shock in the shock frame) and increase in the magnetic field magnitude across the shock are large. Drift acceleration during an encounter can be viewed as resulting from a net displacement (due to an effective grad B drift) of the particle's gyrocenter along the electric field. The energy gained, $\Delta E = q\epsilon\Delta Y$, depends upon the drift distance ΔY, which is a complicated function of the particle's initial velocity, and any wave-particle interactions that occur within a gyroradius of the shock transition (Decker and Vlahos 1985*a*). Energy gains due to drift are fast ($\lesssim$ a few tens of gyroperiods) and can be fairly large ($\sim$10 are more times the initial energy), but in the absence of a return mechanism (e.g., pitch angle scattering) particles will escape the shock and never return. Examples of "pure" drift acceleration are shock spike events observed at laminar, quasi-perpendicular shocks (e.g., Sarris and Van Allen 1974; Decker 1983; Sarris and Krimigis 1985).

2. The first-order Fermi or diffusive shock acceleration mechanism is a statistical process in which particles undergo spatial diffusion along field lines and are accelerated as they scatter back and forth across the shock, thereby being compressed between scattering centers fixed in the coverging upstream and downstream flows (see, e.g., the review by Drury

1983). Energy gains per diffusive cycle (consisting of diffusion from upstream to downstream and back again) are largest at turbulent shocks when $0° \leq \theta_1 \lesssim 45°$ (i.e., the shock is quasi-parallel or parallel [$\theta_1 = 0°$]) because in this range, the difference across the shock between the component of flow parallel to a given field line is largest and, therefore, so is the net energy gain per cycle (e.g., Tsurutani and Lin 1985). An important prediction from diffusive shock acceleration theory is that, at a planar shock with infinite diffusive regions on either side, the steady-state momentum distribution function is a power law in momentum with spectral exponent $\mu_p = 3r/(r-1)$, where r is the compression ratio across the shock. Particles can achieve very high energies by diffusive acceleration, but since particles spend most of their time random walking in the upstream or downstream medium, the acceleration time can become excessively large compared with, for example, the shock's lifetime (e.g., Legage and Cesarsky 1983). Examples of ion events with predominantly diffusive features have been observed at interplanetary shocks (e.g., Scholer *et al.* 1983; Kennel *et al.* 1984; Lee 1983).

3. Low-energy electrons that have gyroradii comparable to or smaller than the shock thickness can interact with the electrostatic turbulence (lower hybrid waves) driven by cross-field currents in the shock transition. As a result of wave-particle interactions, these electrons will diffuse in velocity space and can gain hundreds of keV in energy at quasi-perpendicular shocks (Lampe and Papadopoulos 1975; Tanaka and Papadopoulos 1983).

Since we are interested specifically in ion acceleration at shocks, we shall concentrate on mechanism (1) and (2) above. It is clear that unless the shock is either parallel or perpendicular, both the drift and first-order Fermi processes must be simultaneously operative if a sufficient level of turbulence exists in the shock's vicinity. It is also clear that, in general, intermediate values of θ_1 (i.e., oblique shocks) are likely to prevail in most astrophysical systems. For example, whether one considers (1) an ensemble of planar shocks moving with randomly oriented normals through a uniform field, (2) a single planar shock moving through a magnetic field that is spatially disordered, or (3) a spherical shock expanding into a uniform field, the expectation value of θ_1 is 1 rad, or $\sim 60°$.

Jokipii (1982) was the first to include drift contributions in diffusive shock acceleration theory explicitly by retaining the curvature and gradient drift effects contained in the off-diagonal terms of the spatial diffusion tensor. His solution to the time-independent diffusion equation was obtained by assuming that the drift terms are nonzero only at the shock and that the particle distribution function remains nearly isotropic right at the shock. In addition to predicting that the steady state spectral exponent μ_p is independent of θ_1 (Bell 1978) also reached this conclusion), Jokipii's (1982) solution also predicts that a given energy is related to a unique drift distance ΔY along the shock. As emphasized by Jokipii (1982), this implies that the maximum energy gained is limited at shocks having finite transverse extent. The solution also predicts how the total energy gain is partitioned, on the average, between the first-order Fermi and drift processes for a given θ_1.

In this paper we deal with the problem of time-dependent particle acceleration at turbulent, oblique shocks, and apply our model to the case of prompt ion acceleration during solar flares. In order to treat the general case where θ_1, the level of turbulence, the compression ratio r, and the particle injection energy can assume a range of values, we have performed test particle simulations. This involves numerically integrating along particle phase space orbits in a system composed of a shock with arbitrary θ_1 and predefined spectra of transverse magnetic fluctuations upstream and downstream of the shock. The model incorporates both the shock drift and first-order Fermi processes in a natural way.

Our choice to integrate along particle orbits, as opposed to, for example, invoking the cosmic-ray transport formalism of diffusive shock acceleration theory or performing Monte Carlo simulations (e.g., Ellison 1981) using a specified diffusive coefficient, was prompted by the following considerations. First, we wanted the flexibility to study particle acceleration for shock obliquities and particle injection energies that clearly violate conditions necessary for strict application of the diffusion equation. For example, for particle velocities less than or comparable to that required to transform from the shock frame to the frame where the electric field vanishes on both sides of the shock (the null frame), drift acceleration can produce energy gains and associated pitch angle anisotropies that are very large near the shock (Decker 1983; Webb, Axford, and Terasawa 1983), even in the presence of wave-particle interactions (Decker and Vlahos 1985*a*). Second, and related to the first comment, retaining a particle's instantaneous gyrophase and pitch angle as well as its energy is essential for the proper treatment of drift acceleration. This is especially true when waves are present and the convenient approximation that particles conserve their magnetic moments through a shock encounter is no longer valid (in this situation, there is no unique null frame because of fluctuation in θ_1). Third, orbit integrations are the only way to treat particle transport and acceleration in a field of large-amplitude waves (i.e., $\delta B \approx B_0$), a situation not uncommon at shocks in the solar wind. Finally, we can study the important problem of time-dependent shock acceleration and the evolution of energy spectra as functions of the relevant parameters (i.e., θ_1, r, $\delta B/B_0$). At present, the code is restricted to test particle acceleration at planar, infinitesimally thin shocks.

As a specific application of the simulation code we have considered the acceleration of protons under conditions appropriate to the lower corona during solar flares. The prompt acceleration of ions (and electrons) during solar flares is a classic problem in solar physics for which a model that includes the time-dependent acceleration of particles at a turbulent, oblique shock is particularly well suited. We have found that such shocks formed during solar flares can accelerate an initial population of 100 keV protons to 50 MeV or more in fewer than 10 ms in a 50 G magnetic field (an elapsed time well below the instrumental resolution of existing instruments). Because the shock drift process produces relatively large and fast energy gains, the energy spectra produced at quasi-perpendicular shocks extend $\gtrsim 10$ times higher than those at quasi-parallel shocks within the same elapsed time (all other quantities are held fixed).

The layout of this paper is as follows. In § II we present the basic elements of the simulation model (details are contained in the appendices). In § III we give a brief background on particle acceleration during solar flares, establish appropriate physical parameters for use in the simulation code, and present the numerical results. In § IV we discuss the implication of our results concerning energy versus acceleration time, compare our results for peak energy gained at a parallel shock with predictions from diffusive shock acceleration theory, discuss how our (time-dependent) energy spectra compare with

Jokipii's (1982) steady state solution, and summarize the implications of the simulation results for the prompt acceleration of protons during solar flares, including the effects of Coulomb collisional losses. In § V we give a brief summary of the results.

II. DESCRIPTION OF MODEL

a) Geometry and Main Assumptions

In this section we summarize the physical model used to simulate charged particle interactions with a system consisting of an oblique shock plus magnetic fluctuations on either side of the shock. Specific details are discussed in the appendices. Figure 1 shows the assumed geometry, as well as the relevant reference frames as observed from frame $K(\hat{X}, \hat{Y}, \hat{Z})$ fixed with the shock. We assume that a planar, fast-mode, collisionless MHD shock propagates along its normal $\hat{\boldsymbol{n}}$ with constant velocity $\boldsymbol{V}_s$ through an ambient plasma which in general may be flowing at constant velocity $\boldsymbol{V}_1$, such that $|\boldsymbol{V}_1 \cdot \hat{\boldsymbol{n}}| < |\boldsymbol{V}_s|$. The shock surface coincides with the $(Y\text{-}Z)$-plane, and the upstream (subscript 1) and downstream (subscript 2) plasma bulk flow velocities are $\boldsymbol{U}_1 = \boldsymbol{V}_1 - \boldsymbol{V}_s = (U_1 \cos \delta_1, 0, U_1 \sin \delta_1)$ and $\boldsymbol{U}_2 = (U_2 \cos \delta_2, 0, U_2 \sin \delta_2)$, respectively, with respect to K. Let frames $K_i(\hat{x}_i, \hat{y}_i, \hat{z}_i)$ be those comoving with the upstream and downstream plasmas, such that the unit vectors of the K_i system are $\hat{z}_i = \hat{\boldsymbol{B}}_{0i}$, $\hat{y}_i = \hat{Y}$, and $\hat{x}_i = \hat{y}_i \times \hat{z}_i$, where $\hat{\boldsymbol{B}}_{0i}$ is the unit vector along the mean field $\boldsymbol{B}_{0i}$. For nonrelativistic flows, the magnetic field transforms virtually unchanged from K_i to K and is given by $\boldsymbol{B}_{0i} = (B_{0i} \cos \theta_i, 0, B_{0i} \sin \theta_i)$. The assumption of infinite electrical conductivity implies that any static electric fields in K_i must vanish, so that in K there is the electric field $\boldsymbol{\epsilon}_0 = -\boldsymbol{U}_i \times \boldsymbol{B}_{0i}/c$ that is continuous across the shock (Gaussian cgs units are used throughout).

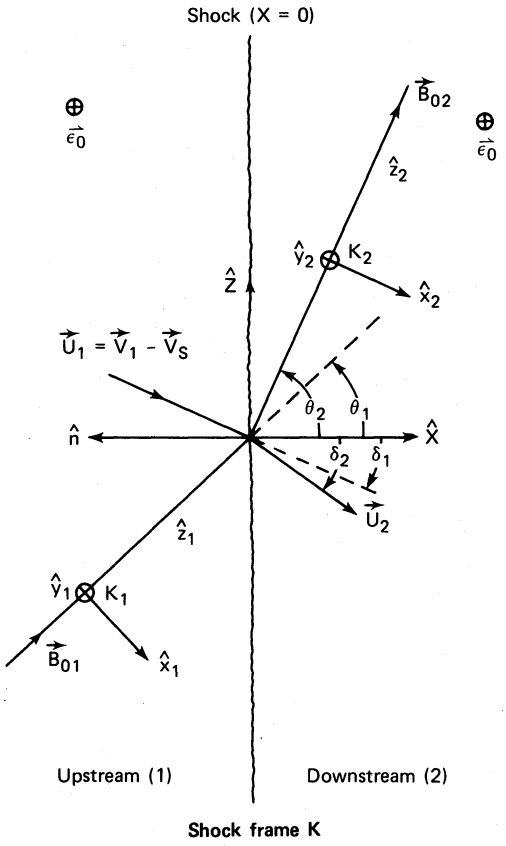

FIG. 1.—Schematic of mean fields and plasma flow velocities in shock frame $K(\hat{X}, \hat{Y}, \hat{Z})$. Frames $K_1(\hat{x}_1, \hat{y}_1, \hat{z}_1)$ and $K_2(\hat{x}_2, \hat{y}_2, \hat{z}_2)$ are fixed in the upstream and downstream plasma, respectively.

Define $M_{A1} = U_1/v_{A1}$ as the Alfvén Mach number, where $v_{A1} = (4\pi\rho_1)^{-1/2} B_{01}$ is the upstream Alfvén speed, $\rho_1 = n_1 m_1$ is the plasma mass density, n_1 is the number density, and m_1 is the ion mass. Also let $\beta_1 = n_1 k_B (T_{1e} + T_{1i})(B_{01}^2/8\pi)^{-1}$ be the upstream plasma beta, where k_B is the Boltzmann constant, and T_{1e} and T_{1i} are the upstream electron and ion temperatures, respectively. For given values of the upstream parameter set $(\theta_1, \delta_1, M_{A1}, \beta_1)$ and the ratio of specific heats γ_r, we obtain the downstream set $(\theta_2, \delta_2, M_{A2}, \beta_2)$ using the MHD jump conditions (Helfer 1952) which, when combined, yield a quadratic equation for the density compression ratio $r = \rho_2/\rho_1$. After factoring out the trivial root $r = 1$, the resulting cubic is solved for r subject to the condition $1 \leq r \leq (\gamma_r + 1)/(\gamma_r - 1)$. The appropriate solution is then used to calculate the other relevant downstream quantities. We assume throughout that we are dealing with an electron-proton plasma, and that $\gamma_r = 5/3$.

In the model we assume the length ordering $d_s \ll \rho \ll R_s, L_s$, where d_s, ρ, R_s, L_s denote, respectively, the shock transition scale (or "thickness"), a test particle gyroradius, the shock radius of curvature, and the spatial extent of the shock in the $(Y\text{-}Z)$-plane. The condition $d_s \ll \rho$ permits us to neglect the electromagnetic microstructure associated with the shock transition, which is apparently valid in the perpendicular and quasi-perpendicular shock regimes when $\rho \gg$ thermal ion gyroradius (Leroy *et al.* 1982). However, in the parallel and quasi-parallel shock regimes, shock transitions are relatively broad, disordered, and poorly defined (Greenstadt and Fredericks 1979). Thus, as compared with the quasi-perpendicular case, meeting the condition $d_s \ll \rho$ requires a higher minimum energy for injected test particles. The planar shock condition $\rho \ll R_s$ allows us to neglect shock curvature effects (e.g., spatially dependent θ_1) as particles drift along the shock surface during shock encounters. Finally, if the shock is of limited scale size L_s in the $(Y\text{-}Z)$-plane, the condition $\rho \ll L_s$ prevents particles from drifting off the shock and out of the acceleration region.

We shall assume that the charged particles of interest are true test particles, that is, they are not self-consistently coupled to the shock or to the wave system, or both. Also we assume there are no loss mechanisms (e.g., Coulomb collisions, radiation, etc.) that might remove a particle from the system or degrade its energy. The validity of this latter assumption is, in principle, testable once the orbit calculations have been performed and quantities such as energy and acceleration time are in hand. This is discussed in § IV for the case of shock acceleration in the low solar corona.

b) Particle Dynamics in the Wave-Shock System

A charged particle injected into the static, uniform system in Figure 1 would encounter the shock only once. In the regime $45° \lesssim \theta_1 \leq 90°$, such an encounter would generally consist of several orbital shock crossings with an energization via drift along $\boldsymbol{\epsilon}_0$ during the encounter (Decker 1983; Webb, Axford, and Terasawa 1983), but then the particle would escape to infinity in the absence of a mechanism to return it to the shock.

To model the situation that involves acceleration by both the shock drift and diffusive processes, we introduce pitch angle scattering by adding a zero-mean, random magnetic field component $\boldsymbol{b}(z) = \hat{x} b_x(z) + \hat{y} b_y(z)$ that, in either plasma frame

K_1 or K_2, varies only with z along $\boldsymbol{B}_0 = \hat{z}B_0$, is transverse to $\boldsymbol{B}_0$, and is time independent (i.e., scattering is elastic in either plasma frame). This form of $\boldsymbol{b}(z)$ insures that $\boldsymbol{B}(z) = \boldsymbol{B}_0 + \boldsymbol{b}(z)$ is divergence-free. Scattering provides a mechanism whereby particles experience multiple shock encounters and can therefore attain high energies through the combination of the shock drift and first-order Fermi processes.

The problem then is to solve, in the appropriate plasma frame, the six, ordinary, first-order, coupled differential equations

$$\dot{\boldsymbol{p}}(t) = (q/c)[\boldsymbol{p}(t)/m] \times \{\boldsymbol{B}_0 + \boldsymbol{b}[z(t)]\} , \quad (1)$$

$$\dot{\boldsymbol{x}}(t) = \boldsymbol{p}(t)/m , \quad (2)$$

for particle position $\boldsymbol{x} = (x, y, z)$ and momentum $\boldsymbol{p} = (p_x, p_y, p_z)$ at time t in either K_1 or K_2, subject to the initial (injection) conditions $\boldsymbol{x}(0)$ and $\boldsymbol{p}(0)$, where $m = \gamma m_0$, $\gamma = [1 + (p/m_0 c)^2]^{1/2}$, and m_0 and q are the particle's rest mass and charge, respectively. The form of equation (1) emphasizes the point that the field $\boldsymbol{b}$ sampled by a particle at time t depends implicitly upon t through the particle's motion along the mean field $\boldsymbol{B}_0$. It is obvious from equation (1) that in either plasma frame the magnitude of the momentum $p = |\boldsymbol{p}|$ or, equivalently, the total energy $W = \gamma m_0 c^2$ or kinetic energy $E = (\gamma - 1)m_0 c^2$ is a constant of the motion. The presence of a static but spatially varying field $\boldsymbol{b}(z)$ in K_1 or K_2 implies that in K the electric field $\boldsymbol{\epsilon} = -c^{-1}\boldsymbol{U} \times \boldsymbol{B}(X, Z, t) = \boldsymbol{\epsilon}_0 + \boldsymbol{e}(X, Z, t)$, where $\boldsymbol{e}(X, Z, t) = c^{-1}\boldsymbol{U} \times \boldsymbol{b}(X, Z, t)$ since $z = z(X, Z, t)$ (see Appendix A). Thus, as viewed from K, particles respond to spatially and temporally varying magnetic and electric fields. We have elected for simplicity to integrate along particle orbits in K_1 or K_2 and perform point Lorentz transformations to K when necessary.

The details of the procedure for integrating equations (1) and (2) are contained in Appendix A. Integration in either plasma frame continues until (*a*) a shock crossing occurs, (*b*) a predefined spatial boundary (i.e., an escape boundary) is crossed, (*c*) a predefined time limit is exceeded, or (*d*) an error condition associated with non-physical behavior is detected. When condition (*a*) occurs, a frame transformation is performed from K_1 to K_2 or from K_2 to K_1, depending upon whether the crossing is from upstream to downstream or from downstream to upstream, respectively, and the integration is continued in the new frame using the transformed position and momentum at $X = 0$ as new initial conditions. When conditions (*b*) or (*c*) are detected, the orbit calculation is stopped, and the particle's phase space coordinates $[\boldsymbol{x}, \boldsymbol{p}]$ are recorded. Condition (*d*) occurs when for some reason (e.g., round-off errors, too large a time step size, etc.) kinetic energy is not conserved in K_1 or K_2, while the particle propagates in either the upstream or downstream regions, respectively. If during its stay in either region the particle's energy change relative to the plasma frame exceeds 5% of its energy at the last crossing, the calculation is aborted, the particle is discarded, and a new particle is injected.

c) *Random Wave Field*

As discussed in detail in Appendix B, we synthesize a realization of the random field $\boldsymbol{b}(z)$ in a slab of width L along z by superposing N monochromatic plane waves. The amplitude of each such Fourier component is determined from a specified power spectrum $P(k)$ in wavenumber k in the interval $[k_S, k_L]$. In this paper we assume that $\boldsymbol{b}(z)$ is composed of circularly polarized Alfvén waves with wave vectors along $\boldsymbol{B}_0$, and we further assume for simplicity that the phase velocity $v_{ph} = v_A = 0$ (v_A is the Alfvén speed), which from the wave dispersion relation $\omega = v_A k$ implies wave frequencies $\omega = 0$. Consequently, we neglect the induced electric field $|\boldsymbol{e}_k| \approx (v_A/c)|\boldsymbol{b}_k|$ of each component with wavenumber k and wave magnetic field $\boldsymbol{b}_k(z)$. Thus, for example, stochastic acceleration in the fluctuating electric field of MHD turbulence (e.g., Kulsrud 1979) is precluded in our model. The neglect of wave phase velocities in the plasma frame is equivalent to neglecting the effect upon particle motion of the wave electric field compared with the effect of the wave magnetic field, an assumption that is valid for particles with speed $v \gg v_A$ (Jokipii 1971), a condition satisfied in our model. The inclusion of time-varying electric and magnetic fields associated with longitudinal and transverse waves is an additional and possibly important complication we do not address, although such studies, not directly related to shock acceleration, have been made for ion propagation in a turbulent plasma environment such as that in the Earth's magnetosheath (Brinca 1984).

d) *Injection Procedure*

We inject particles into the wave-shock system as follows. For a chosen region (upstream or downstream), we choose an injection kinetic energy E_0 and assume an isotropic distribution in momentum space. A particle's initial pitch angle α_0 and gyrophase angle λ_0 are obtained using a random number generator to place the particle on a sphere of radius $p_0 = [E_0(E_0 + 2m_0 c^2)]^{1/2} c^{-1}$, with equal probability of occupying any unit solid angle. Then, $p_{0x} = p_0 \sin \alpha_0 \cos \lambda_0$, $p_{0y} = p_0 \sin \alpha_0 \sin \lambda_0$, and $p_{0z} = p_0 \cos \alpha_0$. Distributions isotropic within an angular interval $\alpha_{01} \leq \alpha_0 \leq \alpha_{02}$ (e.g., beam injections for $\alpha_{01} = 0°$, $\alpha_{02} \lesssim 30°$) are easily obtained by discarding particles outside that range. Injection positions $\boldsymbol{x}_0$ are obtained by placing the guiding center of each particle at the same point, this point being at least one gyroradius ρ_0 from the shock surface. A different realization of $\boldsymbol{b}(z)$ can be used for each particle. However, since the conditions $h_b \ll z_c \ll L$ and $\rho_0 \approx h_b$ are generally met in our simulations, we saved computer time by keeping the sample realization for 100 particles and simply shifting the origin of the realization by a random length between 0 and L, while maintaining periodic boundary conditions as described in Appendix B. This technique produces particle distributions that do not differ in a statistical sense from those obtained by using a different realization for each particle.

III. PROMPT ACCELERATION OF IONS IN SOLAR FLARES

a) *Background*

Solar flares often accelerate ions and electrons to very high energies. The details of the acceleration processes are not well understood (Vlāhos *et al.* 1985), but until recently the main trend was to divide the acceleration process(es) into two phases (see detailed discussion by Ramaty *et al.* 1980). During the first phase, electrons are heated and accelerated up to several hundreds of keV simultaneously with the energy release. These mildly relativistic electrons interact with the ambient plasma and magnetic field and generate X-ray and radio emission. During the second phase, usually delayed from the first phase by several minutes, ions and relativisitic electrons are accelerated. Thus, particles accelerated during the first phase serve as a seed population for the second phase. These ions and relativistic electrons can interact with the solar atmosphere, generating gamma-ray continuum, gamma-ray line, and neutron

emission, or they can escape into interplanetary space. In several flares, the second phase coincides in time with the start of a type II burst in radio emission, which is believed to be the signature of a shock wave (see Frost and Dennis 1970).

The theoretical work on particle acceleration during solar flares has also emphasized the two-phase acceleration scheme, and various acceleration mechanisms have been proposed. During the first phase, DC electric fields, resistive heating, and wave acceleration can energize the electrons and ions (Vlahos *et al.* 1985). During the second phase, ions and relativistic electrons can be accelerated by MHD turbulence, shock waves, or both (see, e.g., Barbosa 1979; Ramaty 1979; Acterberg and Norman 1980; Melrose 1983). Achterberg and Norman (1980) suggested that the delay between the first and second phase is due primarily to the fact that the shock is initially formed in the low, dense corona ($n = 10^{11}$ cm^{-3}) where the rate of energy gain by diffusive acceleration at parallel shocks is less than the rate of energy loss due to Coulomb collisions. Thus, the shock must travel several scale heights before becoming an efficient accelerator. Ellison and Ramaty (1985) used the diffusive acceleration theory at parallel shocks to analyze the spectra of electrons, protons, and alpha particles for several solar energetic particle events and found that for each major event a unique shock compression ratio in the range $r = 1.5$–3 produces spectra in good agreement with observations.

It has been proposed (Bai *et al.* 1983) that $\sim$100 keV electrons accelerated near the top of a magnetic loop can precipitate along the legs of the loop and heat the dense chromospheric plasma. The "evaporated" portion of the dense chromospheric plasma will stream toward the corona along the loop and will form two counterstreaming hydrodynamic "shocks." Bai *et al.* (1983) conjecture that if 1 MeV protons preexist in the loop, they will undergo further acceleration at the counterstreaming "shocks." Smith and Brecht (1985) studied this scenario and concluded that the shock formation time is $\sim$2 s. They also concluded that particle acceleration above 3 MeV is unlikely unless the shocks become turbulent, and particle trapping between the two converging shocks is maintained by scattering in this turbulence rather than by simple adiabatic mirror reflections which occur at laminar, oblique shocks.

The two-phase acceleration scenario was questioned recently in light of results from the Gamma-Ray Spectrometer (GRS) aboard the *Solar Maximum Mission*. In several flares (Chupp 1984), particles were accelerated to energies up to 100 MeV in fewer than 2 s (the resolution of the instrument). These new results posed an important theoretical question: How fast are shocks and MHD turbulence formed and how quickly can they accelerate ions to 50 MeV or more in the solar corona? We address this question below.

b) Shock Model and MHD Turbulence Spectrum

We analyze the acceleration of ions by using the following model. We assume that during a flare, magnetic energy is converted to particle energy through heating of the bulk plasma and acceleration of particles in the tail of the plasma distribution. The high plasma pressure inside the energy release volume expands in all directions since the plasma beta exceeds unity. A piston-driven perpendicular or oblique shock is formed in a few microseconds (Papadopoulos *et al.* 1985). We assume that the flare-driven oblique shocks are embedded in MHD turbulence upstream and downstream of the shock. These small-scale, pressure-driven shocks that are formed in the vicinity of the energy release volume should not be confused with the large-scale coronal shocks that are responsible for the type II bursts. The correlation between such large-scale shocks and those discussed here is an important problem, but is beyond the scope of this paper. The shock and plasma parameters used in all computer runs discussed in this paper are listed in Table 1. Since θ_1 is the only parameter that was varied from run to run, we also list in Table 1 the relevant downstream quantities and the theoretical slope of the energy spectrum (§ IV) for each θ_1 used.

We now address two important questions. First, what is the source of the MHD turbulence we have assumed in our model? Second, do we expect oblique shocks to be formed in solar flares? As to the first question, we note that the source(s) and spectral form of MHD turbulence are, of course, largely unknown in the vicinity of a flare-driven shock. Possible sources of the upstream turbulence include the turbulent preflare plasma and Alfvén waves driven by energetic ($\gtrsim$100 keV) ion beams streaming upstream from the shock following reflection from the shock or from leakage from the hot flare plasma downstream, or from both. The excitation of Alfvénic turbulence from ion beams has been discussed extensively in relation to the wave-particle activity upstream of the Earth's bow shock (see, e.g., Gary, Gosling, and Forslund 1981; Gary 1985; Sentman, Kennel, and Frank 1981; Winske and Leroy 1984). Possible sources downstream include the upstream turbulence

TABLE 1

INPUT AND DERIVED PARAMETERS FOR SIMULATION OF ACCELERATION AT SOLAR FLARE SHOCKS

A. UPSTREAM

INPUT

Parameter	Value
U_1	3.3×10^8 cm s^{-1}
B_{01}	50 G
θ_1	0°, 15°, 30°, 45°, 60°, 75°
δ_1	0°
n_1	10^{10} cm^{-3}
$T_{1e} + T_{1i}$	10^7 K

DERIVED

Parameter	Value
v_{A1}	1.1×10^8 cm s^{-1}
M_{A1}	3
β_1	0.14
Ω_{01}	$eB_{01}/m_{0p}c = 4.8 \times 10^5$ s^{-1}
τ_{01}	$2\pi/\Omega_{01} = 1.3 \times 10^{-5}$ s

B. DOWNSTREAM[a]

θ_1	θ_2	δ_2	B_2/B_1	$r = \rho_2/\rho_1$	U_2/U_1	Γ
0°	0°	0°	1.00	3.85	0.26	1.03
15	54	22	1.64	3.58	0.30	1.08
30	67	35	2.20	3.22	0.34	1.18
45	74	21	2.50	3.00	0.36	1.25
60	79	15	2.63	2.83	0.37	1.32
75	85	8	2.70	2.75	0.37	1.36

[a] All parameters derived.

convected through and amplified by the shock, as well as turbulence excited by the flare release mechanism.

Figure 2 shows the spectral form $P(k)$ assumed for all computer runs (see Appendix C). The spectrum extends from wavenumber k_S to k_L, has a correlation length z_c, and exhibits a spectral slope $= -5/3$ for $k \gg z_c^{-1}$. For $\boldsymbol{b}(z) = \hat{x}b_x(z) + \hat{y}b_y(z)$ we set $\tilde{\sigma}_x^2 = \tilde{\sigma}_y^2 = \tilde{\sigma}^2/2$, where $\tilde{\sigma}^2$ is the variance of the total random field defined by equation (C6). For the quantities described in Appendix B we set $p = 12$, $q = 6$, and $z_c = 10^5$ cm, so the number of Fourier components that comprise $b(z)$ is $N = 2^{12} = 4096$, the realization length $\tilde{L} = L + h_b = 2^6 z_c = 6.4 \times 10^6$ cm, the grid spacing $h_b = 2^6/z_c = 1.56 \times 10^3$ cm, $k_S = 9.8 \times 10^{-7}$ cm, and $k_L = 2.0 \times 10^{-3}$ cm. The function $P(k)$ was evaluated for each Fourier component and was used along with randomly generated phases to synthesize a particular realization of $\boldsymbol{b}(z)$. Input values $\tilde{\sigma}_1^2 = 0.2$ upstream and $\tilde{\sigma}_2^2 = 0.4$ downstream yielded actual variances of $\sigma_1^2 = 0.19$ and $\sigma_2^2 = 0.38$ upon statistical analysis of $b(z)$. Figure 2 shows the upstream spectrum for $B_0 = B_{01} = 50$ G. Note that the chosen spectral form provides power for resonant pitch angle scattering (i.e., proton gyroradius $\sim k^{-1}$) of protons (top scale of Fig. 2) with energies spanning the range of flare-associated energies from 100 keV to 10 GeV. We set the escape length Λ_i (Appendix A) and field damping length X_i^d (Appendix B) to 10^8 cm, so that virtually no particles escape during a typical run.

Now, in response to the second question posed above, we note that the angle θ_1 between the magnetic field upstream of the shock and the shock normal depends strongly on the geometry of the ambient magnetic field in the vicinity of the flare energy release. In Figure 3 we show three simplified flare models (Sturrock 1980). A quasi-perpendicular shock will be formed at the top of an emerging flux tube (Fig. 3*a*), a quasi-parallel shock will be formed when a shock propagates along a coronal streamer (Fig. 3*b*), and finally an oblique shock will be formed when several loops interact to produce a shock that expands against an upstream magnetic field that is randomly oriented. In this latter case the average angle between the shock normal and the ambient upstream magnetic field is

$$\langle \theta_1 \rangle = \frac{1}{2\pi} \int_0^{2\pi} d\phi \int_0^{\pi/2} \theta_1 \sin \theta_1 d\theta_1 \approx 57°.$$

It is clear that oblique shocks can be formed in the topologies shown in Figures 3*a* and 3*b* if the field and shock surface are not perfectly aligned. We conclude that oblique shocks are probably common in solar flares. In addition, when MHD turbulence in the form of parallel propagating Alfvén waves is added, θ_1 can change radically with time. For example, in the lower panel of Figure 4 we show the x-component $b_x(z)$ for a short segment of a realization of $\boldsymbol{b}(z)$ as a function of distance z (in units of z_c) along the mean field (note $\sigma_x^2/B_0^2 = 0.1$). The upper panel shows the difference $\theta(z) - \theta_0$ between the instantaneous value of $\theta(z)$ and the mean value θ_0. Although $\theta(z)$ averages to θ_0 over the entire realization, fluctuations about θ_0

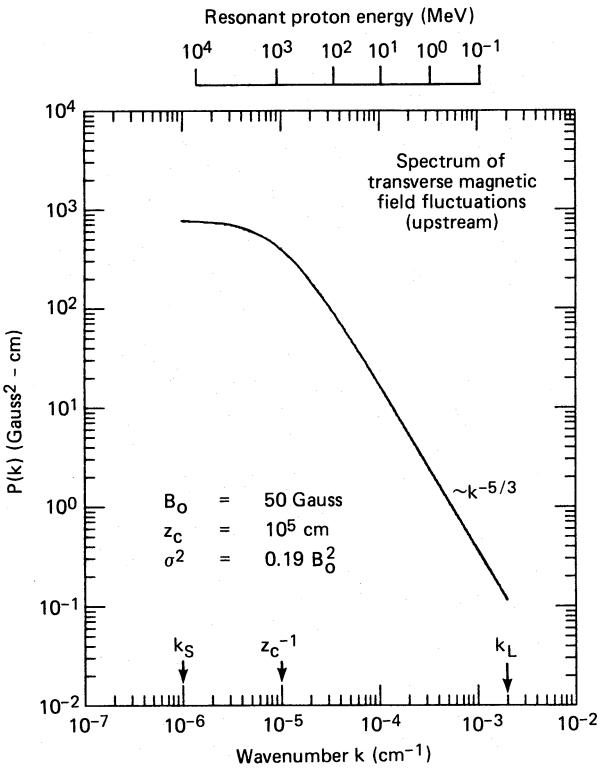

FIG. 2.—Wave number power spectrum assumed for simulations of proton acceleration at coronal shocks. For the upstream region shown here, the mean magnetic field strength $B_0 = 50$ G, the correlation length of the power spectrum $z_c = 10^5$ cm, and the variance $\sigma^2 = 0.19B_0^2$. The scale at the top shows the kinetic energy of protons with gyroradii $\rho = k^{-1}$, indicating the power available for resonant pitch angle scattering.

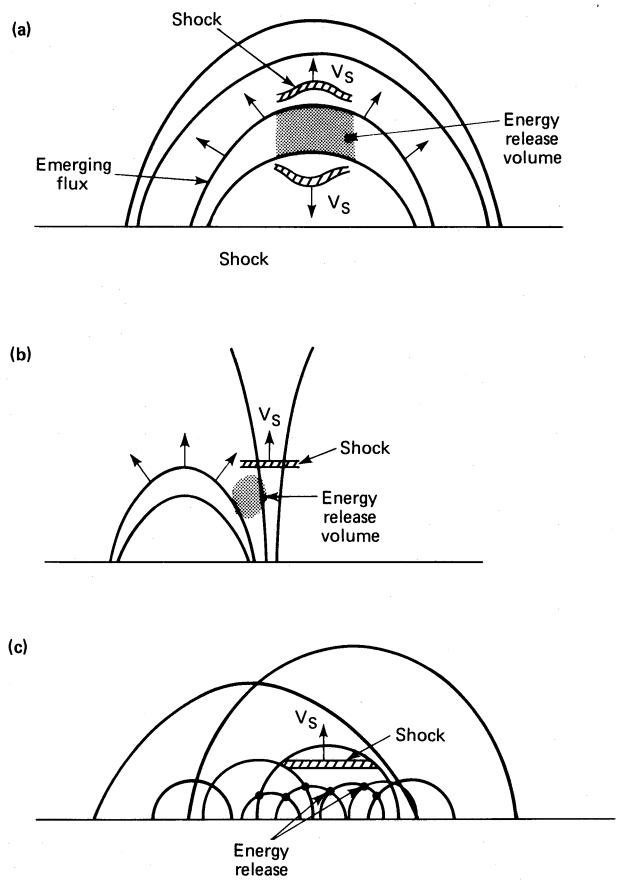

FIG. 3.—Schematics of three simplified flare models and associated shock geometries: (*a*) formation of quasi-perpendicular shocks at the top of a magnetic loop; (*b*) formation of quasi-parallel shock along coronal streamer; (*c*) formation of oblique shock by several interacting loops.

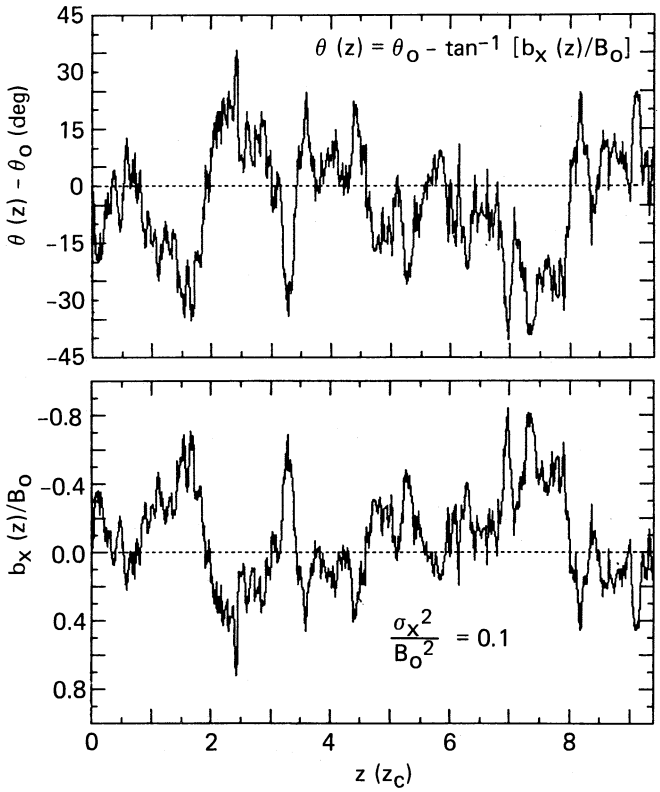

FIG. 4.—*Bottom:* Sample of x-component of random magnetic field realization along z-axis (mean field direction) in units of correlation length z_c of the power spectrum. *Top:* Difference between instantaneous angle $\theta(z)$ and mean angle θ_0 between magnetic field and shock normal as a result of fluctuations $b_x(z)$ in bottom panel.

of $\sim 20^\circ \approx \sigma_x/B_0$ or more are common. These fluctuations are significant to charged particles that respond to the local field and therefore the local θ, not θ_0, at shock crossings.

c) *Numerical Results*

Figures 5 and 6 show sample proton trajectories for mean angles $\theta_1 = 15^\circ$ and $\theta_1 = 60^\circ$, respectively. The protons were injected upstream with energy $E_0 = 100$ keV measured in the upstream plasma frame. We define the scale time $\tau_{01} = eB_{01}/m_0 c = 1.3 \times 10^{-5}$ s (nonrelativistic upstream gyroperiod) and scale length $\rho_{01} = v_0 \tau_{01}/2\pi = 9.1 \times 10^2$ cm (upstream gyroradius of a 100 keV proton with speed 4.4×10^8 cm s^{-1}). In Figures 5*a* and 6*a* kinetic energy E (in units of E_0) in the shock frame is shown versus distance X/ρ_{01} from the shock (upstream at left, downstream at right of dashed line at $X = 0$). The elapsed time of each orbit is given at the top of Figures 5*a* and 6*a*. An alternate representation of the orbits is given in the right side of Figures 5 and 6, where in Figures 5*b*, 6*b* and 5*c*, 6*c* E/E_0 and X/ρ_{01}, respectively, are shown versus time t/τ_{01}. Periods A–I in Figure 5*a* and A–H in Figure 6*a* are indicated by the corresponding symbol at the top of Figures 5*b* and 6*b*, respectively. In Figures 5*a* and 6*a* the upstream magnetic fluctuations convect toward the shock from the left with speed U_1, and the downstream magnetic fluctuations convect away from the shock with speed $U_2 < U_1$ (Table 1).

For the case $\theta_1 = 15^\circ$ (i.e., quasi-parallel shock) in Figure 5, energy gains result primarily from the first order Fermi process, i.e., diffusive acceleration. There are four episodes ($t/\tau_{01} \approx$ 0–85, 125–175, 180–220, and 220–260) where the particle escapes upstream with mean energy E_i, is scattered through 90° pitch angle in the incoming wave field (periods A, D, F, and H), and returns to the shock with mean energy E_f. We estimate the maximum energy gains in each of these episodes and compare them with Figure 5 using the following simple argument. Although the process whereby a charged particle gains energy in the shock frame by scattering off the convecting wave field is electrodynamic, we consider the mechanical analog of a particle constrained to move along a wire [the mean field $\boldsymbol{B} = B_0(\cos\theta, 0, \sin\theta)$] along which are fixed massive scattering centers (magnetic fluctuations). If in the laboratory frame (shock frame K) the wire is moving with velocity $\boldsymbol{U} = U(\cos\delta, 0, \sin\delta)$, then the component of U along B_0 is $U_\parallel = U\cos(\theta - \delta)$. Assuming nonrelativistic motion, the change in the particle's speed along $\boldsymbol{B}_0$ after undergoing elastic scattering in the moving wire frame (plasma frame) is $\Delta v = v_f - v_i = \pm 2U_\parallel$, so

$$E_f = mv_f^2/2 = E_i \pm 2mv_i U_\parallel + 2mU_\parallel^2 ,$$

or

$$(E_f - E_i)/E_0 = \Delta E/E_0 = 4(U_\parallel/v_0)[U_\parallel/v_0 \pm (E_i/E_0)^{1/2}] ,$$

where v_0 is the injection speed and the upper and lower signs indicate scattering off approaching (energy gain) or receding (energy loss) scattering centers, respectively. Inspection of Figure 5 shows that for the four energy gain episodes (A, D, F, and H), $E_i/E_0 \approx 2$, 8, 20, and 33, $E_f/E_0 \approx 5$, 17, 30, and 48, so $\Delta E/E_0 \approx 3$, 9, 10, and 15. For $\theta_1 = 15^\circ$, $\delta_1 = 0^\circ$, and $U_1 = 3.3 \times 10^8$ cm s^{-1}, $U_\parallel/v_0 = 0.72$ for $E_0 = 100$ keV, and using the upper sign in the above equation yields $\Delta E/E_0 \approx 6$, 10, 15, and 19, in reasonable agreement with the simulation results. Note that the estimated energy gains are consistently larger than those in Figure 5 since we have neglected the effect of finite pitch angle, so the actual change in parallel velocity is generally smaller than the maximum value of $2U_\parallel$ used above.

There are also three episodes of energy loss (B, C, and I) in Figure 5 due to scattering off receding downstream waves. Inspection of Figure 5 reveals that $E_i/E_0 \approx 5$, 12, and 47, $E_f/E_0 \approx 4$, 10, and 43, so $\Delta E/E_0 \approx -1$, -2, and -4. For $\theta_2 = 54^\circ$, $\delta_2 = 22^\circ$, $U_2 = 8.6 \times 10^7$ cm s^{-1} (Table 1), $U_\parallel/v_0 = 0.17$, and using the lower sign in the above equation yields $\Delta E/E_0 \approx -1.4$, -2.2, and -4.5, again in reasonable agreement with the simulation results. The fact that the energy gained by scattering off approaching upstream waves exceeds that lost by scattering off receding downstream waves over a cycle of motion from upstream to downstream and back again is the simple physical process responsible for diffusive shock acceleration (Bell 1978). However, we should stress that even for $\theta_1 = 15^\circ$, there are abbreviated episodes of shock drift acceleration ($t/\tau_0 \approx$ 100–105 and period E) or direct reflection from the shock (periods E and G), or both. The second process serves to reinject particles directly back upstream, thereby bypassing the downstream energy-loss portion of the diffusive cycle.

For the case $\theta_1 = 60^\circ$ (i.e., quasi-perpendicular shock) in Figure 6, energy gains result primarily from shock drift acceleration. There are three major episodes ($t/\tau_{01} \approx$ 0–4, 52–54, and 60–62) of rapid acceleration during drift along the shock, as well as two other periods ($t/\tau_{01} \approx 12$ and 37–39) of direct reflection accompanied by smaller energy gains. There are also two episodes of first-order Fermi energy gains ($t/\tau_{01} \approx$ 12–37

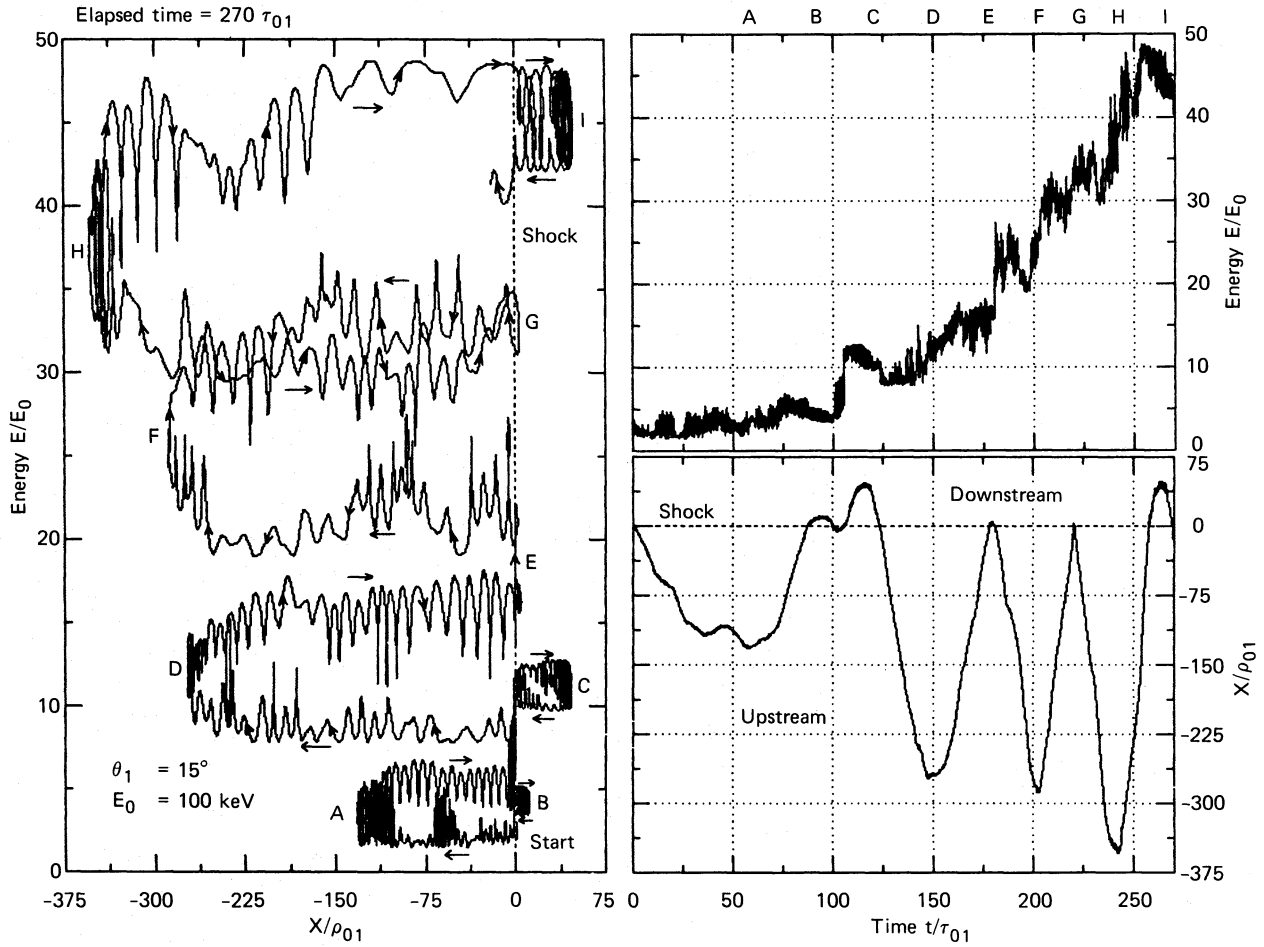

FIG. 5.—Sample orbit for quasi-parallel shock $\theta_1 = 15°$. *Left:* energy vs. X orbit in shock frame, where X is the distance from the shock ($X < 0$ upstream; $X > 0$ downstream). Elapsed time of orbit is $270\tau_{01}$. *Right:* evolution of energy (*upper*) and X-component of particle's position vs. time. Points A–I marked along orbit in left panel are indicated at the top of the right panels. See text for details.

and 39–47) and three episodes of small energy losses ($t/\tau_{01} \approx$ 47–49, 49–52, and 54–60). However, the striking feature of Figure 6 is that the fastest (~few gyroperiods) and largest energy gains occur during the drift phases of acceleration. In comparison, the diffusive gains are relatively slow (~tens of gyroperiods) and small. The particle at the 60° shock gained nearly 5 times more energy than that at the 15° shock ($E/E_0 \approx$ 185 vs. 40) and did so in less than one-fourth the time ($t/\tau_{01} \approx$ 65 vs. 270).

The particles shown in Figures 5 and 6 are among those that underwent the largest energy gains at the 15° and 60° shocks, respectively. However, they are representative examples of the basic physics involved in the diffusive and shock drift processes, and also nicely illustrate how each process predominates in the quasi-parallel and quasi-perpendicular shock geometries, respectively. This latter point is even more apparent in Figure 7, where we have plotted energy E (in units of E_0 on left axis, in MeV on right axis) versus acceleration time t_a/τ_{01} after a total elapsed time of $500\tau_{01} = 6.6$ ms for each of ~2100 protons injected at shocks with $\theta_1 = 0°$, 15°, 30°, 45°, 60°, and 75° (all other parameters held fixed). Plotted is the total energy against the time taken to reach that energy, or equivalently, the time of the particle's last shock crossing. Points with $t_a/\tau_{01} < 500$ imply that these particles spent the time $500 - t_a/\tau_{01}$ diffusing without net energy change in the upstream or downstream regions. We shall discuss this and the following figures more fully in § IV.

Figure 8 shows energy spectra produced by binning the single particle results of Figure 7. The quantity $\Delta f/\Delta E$ is the fraction of particles with energy E within ΔE centered on the logarithmically spaced plot points. For easy comparison, the spectra are shown separated from the unshifted 0° case by factors of 10, increasing from 10^1 at 15° to 10^5 at 75°. Each spectrum includes both upstream and downstream particles. For reference, the fraction of particles left downstream after 6.6 ms is 0.72, 0.74, 0.71, 0.81, 0.94, and ~1.0 for $\theta_1 = 0°$, 15°, 30°, 45°, 60°, and 75°, respectively. Statistical standard deviations, significant only at the highest energies, are within twice the size of the plot point. By requiring a minimum of 10 particles per energy interval, we excluded from Figure 8 the few highest energy particles in Figure 7. Figure 9 shows the fraction of particles from Figure 7 with energy above that indicated on each curve as a function of θ_1. Only fractions above the 10^{-2} level (≥20 particles) are shown.

IV. DISCUSSION

In this section we discuss the effects of shock obliquity on acceleration rate, compare specific results from the simulation with those predicted by existing theoretical models, and esti-

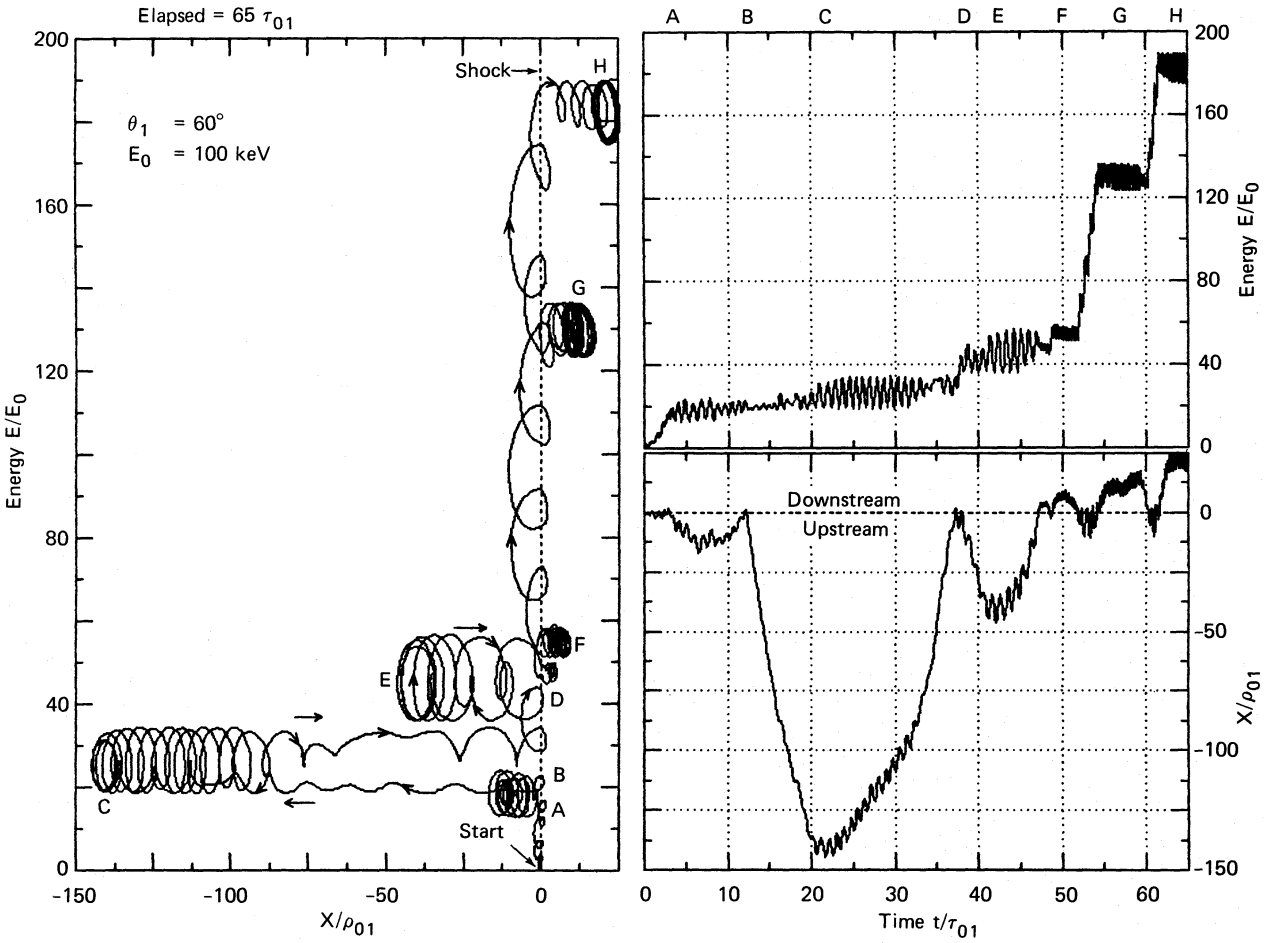

FIG. 6.—Sample for quasi-perpendicular shock $\theta_1 = 60°$. See Fig. 5 caption and text for details.

mate the effects of Coulomb collisional losses during shock acceleration.

a) Energy versus Acceleration Time

Figures 7, 8, and 9 reveal the following features. (1) The percentage of protons accelerated above 10 MeV within 6.6 ms increases with increasing θ_1, from 0% at $\theta_1 = 0°$ to a maximum of 9% at $\theta_1 = 60°$. (2) The case $\theta_1 = 75°$ produces the largest, most rapid energy gains, with $\sim 1\%$ of the protons accelerated above 50 MeV. (3) As θ_1 increases from 0° to 75°, the fraction of particles available for further acceleration steadily declines (note the logarithmic time scale), as indicated by the decrease in the density of points near the 6.6 ms cutoff. For $\theta_1 = 75°$, and to some extent, for $\theta_1 = 60°$, there is a dropout of points at lower energies for $t_a/\tau_{01} \gtrsim 60$; thus, at 75°, the spectrum from 100 keV to $\gtrsim 10$ MeV was completed within 6.6 ms. (4) For $\theta_1 = 75°$, 60°, and, to some extent, 45°, a separate proton population extending to ~ 10 MeV was accelerated during superfast phase, with an upper energy cutoff indicated by the dashed diagonal lines. In summary, the energy distribution produced during a finite acceleration time is a strong function of θ_1, with the first-order Fermi and shock drift processes predominating in the quasi-parallel and quasi-perpendicular shock geometries, respectively.

An important dimensionless parameter in the study of shock drift acceleraton at oblique shocks in the scatter-free limit is the ratio V_N/v. Here v is the particle velocity and $V_N = U_1 \sec \theta_1$ is the transformation velocity along $\boldsymbol{B}_{01}$ from the upstream plasma frame to the null electric field frame where the convection electric field vanishes identically on both sides of the shock [such a Lorentz transformation is possible as long as $\theta_1 < \theta_{1c} = \cos^{-1}(U_1/c) \geq 89°.4$ for $U_1/c \leq 10^{-2}$]. The ratio V_N/v_0, where v_0 is the injection velocity of 100 keV protons, is plotted in Figure 10*a* (left-hand axis) versus θ_1. The right-hand axis shows the ratio of the associated energies. The ratio V_N/v_0 varies from 0.75 to 2.9, from $\theta_1 = 0°$ to 75°. It is well known that the scatter-free shock drift process yields the largest energy gains per shock encounter when $V_N/v_0 \approx 1$ (e.g., Decker 1983; Webb, Axford, and Teresawa 1983). In this case, peak energy gains per encounter at quasi-perpendicular shocks can be several times larger than the initial energy. When a spectrum of waves is added, peak energy gains per shock encounter can in turn be several times larger than those in the scatter-free case (e.g., Fig. 6). This occurs because of spatial and temporal fluctuations in θ_1 (Fig. 4) and because of pitch angle scattering during drift acceleration (Decker and Vlahos 1985*a*). As a result, a small fraction of particles can gain up to ~ 100 or more times their initial energy during essentially one encounter with a quasi-perpendicular shock. The superfast ($t_a/\tau_{01} \lesssim 10$) energization from 100 keV to ~ 10 MeV for $\theta_1 = 45°$, 60°, and 75° in Figure 7 results from such intense drift acceleration following injection at optimum velocities $v_0 \approx V_N$.

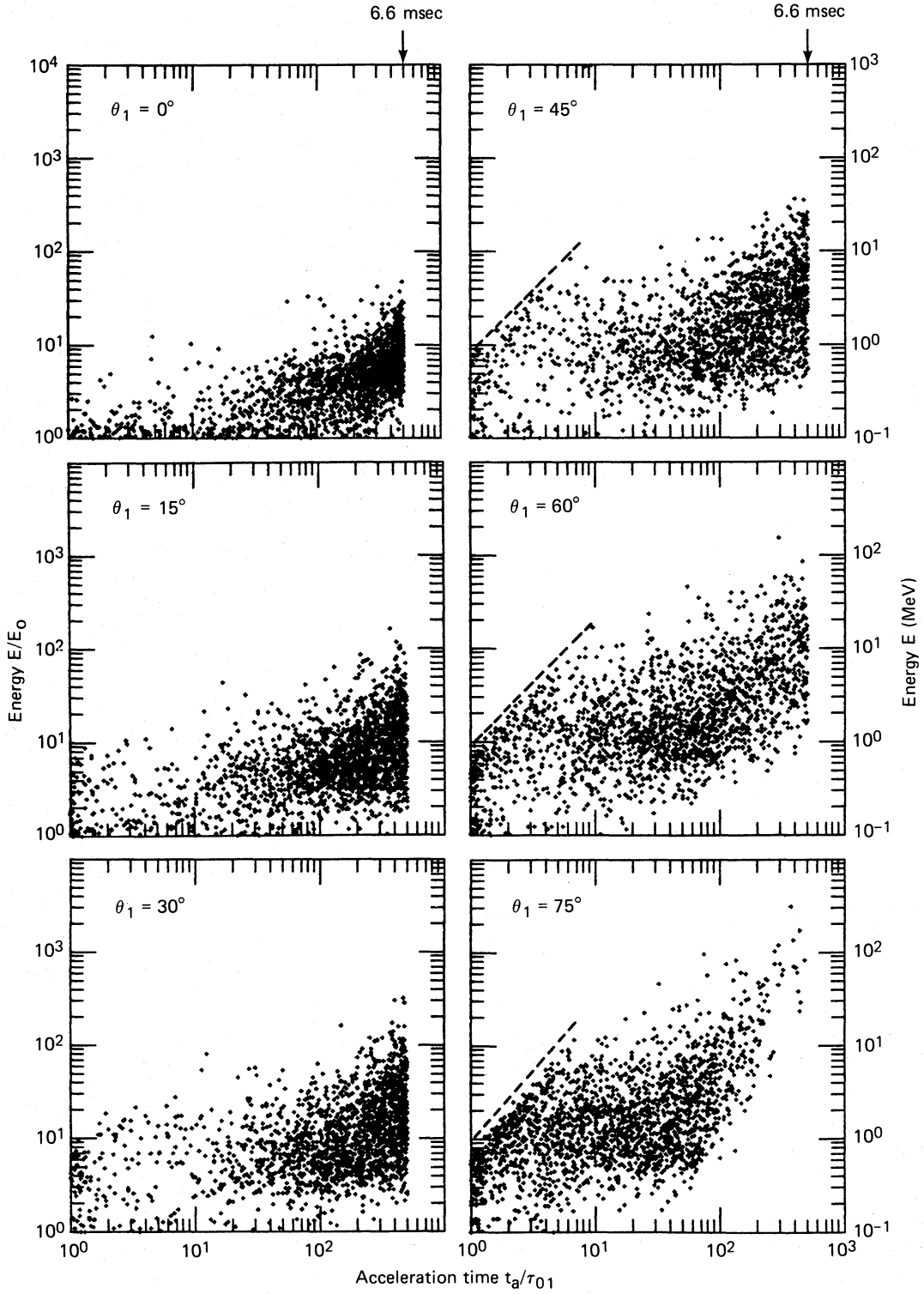

FIG. 7.—Plots of kinetic energy E (in units of injection energy E_0 on left axes, in MeV on right axes) vs. acceleration time t_a in units of upstream gyroperiod τ_{01}. Simulation cutoff time of $500\tau_{01} = 6.6$ ms is indicated at top. Roughly 2100 particles for each of six values of θ_1 (all other parameters held fixed) are shown. Although each particle spent $500\tau_{01}$ in the system, t_a is the time of the particle's last shock crossing, and, therefore, the particle's effective acceleration time.

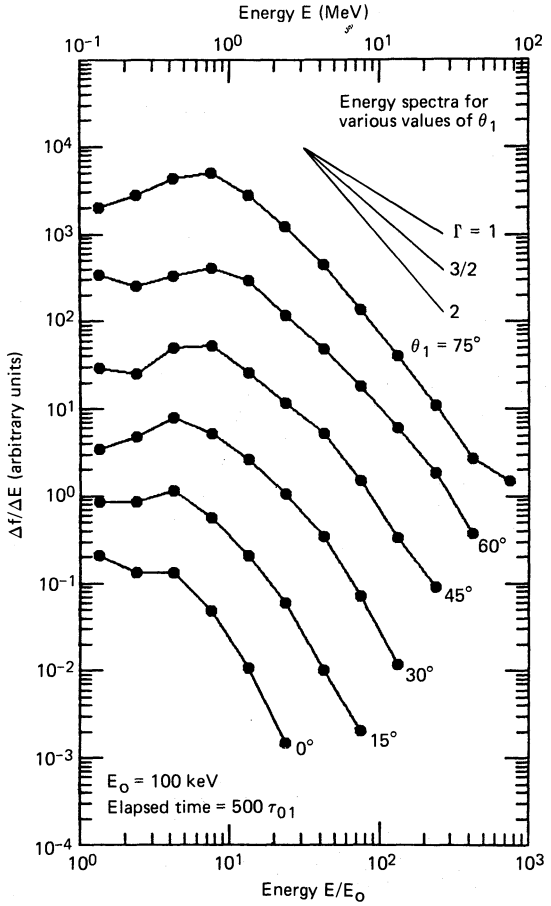

FIG. 8.—Energy spectra produced by binning single particle results in Fig. 7. Spectra are separated from the unshifted 0° case by factors of 10 increasing from 10^1 at 15° to 10^5 at 75°. Statistical standard deviations are within twice the width of the plot points. A scale for spectral slopes between 1 and 2 is also included.

It is important to note that the statistical fluctuations in θ_1 and, therefore, V_N imply the nonexistence of a Lorentz transformation to any global null frame. Specifically, as the rms amplitude δB of the random field increases from zero, the use of a null frame based upon the mean value of θ_1 becomes increasing suspect. When $\delta B \approx B_0$, the null frame and concepts associated with it, such as conservation of particle magnetic moments and energy during shock encounters, are meaningless.

For a given turbulence level, the shock obliquity also plays an important role in determining how easily particles can reencounter the shock. This effect is illustrated in Figure 10*b*. We assumed for simplicitly that particles with the indicated speeds (v/v_0 = 2, 5, and 10) escaped the shock beamed along the mean upstream or downstream magnetic fields. Plotted as a function of θ_1 is the maximum change in pitch angle $\Delta\alpha_{max}$ required for the particle to reencounter the shock from upstream (left axis) or downstream (right axis). This is the maximum pitch angle change because particles generally escape the shock with a range of finite pitch angles. For example, when $v/v_0 = 2$, a particle that escapes upstream must scatter through $\sim 68°$ for $\theta_1 = 0°$ and $\sim 40°$ for $\theta_1 = 60°$ in order to reencounter the shock; however, for $\theta_1 > 68°$, $v < V_N$, so escape upstream is kinematically impossible. If the same particle were to escape downstream, it must scatter through $\sim 112°$ for $\theta_1 = 0°$ and through $\sim 140°$ for $\theta_1 = 60°$ in order to catch up with and reencounter the shock; again, for $\theta_1 > 68°$, $v < V_N$, so once left downstream, this particle can never reencounter the shock.

As v/v_0 in Figure 10*b* increases, V_N/v decreases [except for nearly perpendicular shocks where $\theta_1 \approx \cos^{-1}(U_1/v)$], and the upstream/downstream asymmetry decreases as $\Delta\alpha_{max}$ approaches 90° in each region over a large range of θ_1. The main point is that in the quasi-perpendicular regime injected particles can rapidly attain high energies by successive episodes consisting of reflection upstream and scattering back to the shock, since the necessary scattering angle is relatively small and the energy gain at reflection is relatively large. However, once transmitted through the shock, the particle has a difficult time returning to the shock since the particle must scatter through a relatively large angle in order to reencounter the receding shock. This scenario is supported by features in detailed orbit plots and the distribution in Figure 7.

Finally, we note that due to fluctuations in θ_1 about its mean value, particles may find it easier or harder to reencounter the shock as compared to the situation where θ_1 is the mean angle. Particles that undergo multiple shock encounters will generally see a different θ_1 at each encounter. These fluctuations are particularly important at quasi-perpendicular shocks where small variations in θ_1 produce large variations in V_N through its dependence upon sec θ_1. This provides an additional statistical element that is not contained in solutions of the standard transport equation as applied to shock acceleration.

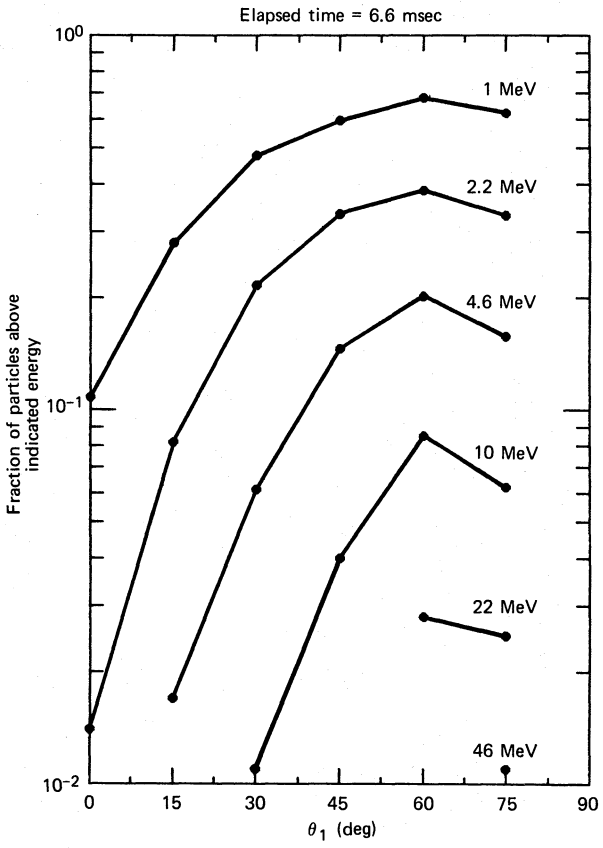

FIG. 9.—Fraction of particles from Fig. 7 with energy above the level indicated vs. angle θ_1. Only fractions above 10^{-2} level (≥ 20 particles) are shown.

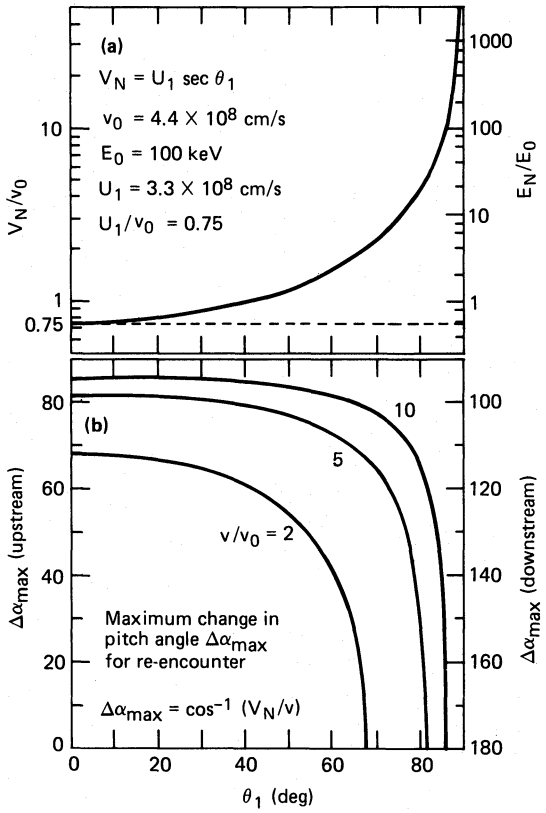

FIG. 10.—(*a*) Ratio of the transformation velocity V_N to the injection velocity v_0 of 100 keV protons. The quantity V_N is the transformation velocity along the mean upstream magnetic field from the upstream plasma frame to the frame where the electric field vanishes on both sides of the shock. The right-hand axis shows the ratio of the associated energies. (*b*) Maximum change in pitch angle required for particles with the indicated velocities to reencounter the shock after escaping upstream (*left*) or downstream (*right*) beamed along the mean magnetic field.

b) Peak Energy Gain at a Parallel Shock

Diffusive shock acceleration theory provides an estimate of the maximum energy attainable after a finite acceleration time at a parallel shock. If Δp and Δt are, respectively, the mean momentum change and mean time taken per cycle (one cycle involves diffusion from upstream to downstream and back again), then the rate of change of momentum due to first-order Fermi process is (e.g., Legage and Cesarsky 1983; Drury 1983)

$$\frac{\Delta p}{\Delta t} \approx \frac{U_1 - U_2}{3(\kappa_1/U_1 + \kappa_2/U_2)}\, p\,, \tag{3}$$

where κ_1 and κ_2 are the upstream and downstream spatial diffusion coefficients parallel to the mean field, respectively. For a wave field consisting of a spectrum of circularly polarized Alfvén waves with wave vectors parallel and antiparallel to the mean field $\boldsymbol{B}_0$, the pitch angle diffusion coefficient obtained from quasi-linear theory (e.g., Jokipii 1971; Wentzel 1974) is given by

$$D_{\mu\mu} = \frac{\pi}{4}(1-\mu^2)\Omega_0 \frac{kP(k)}{B_0^2}\,, \tag{4}$$

where $\mu = \cos\alpha$ (α is the pitch angle measured relative to $\boldsymbol{B}_0$), $P(k)$ is the wavenumber power spectrum (e.g., eq. [C1]), and $\Omega_0 = qB_0/(mc)$ is the gyrofrequency. Equation (4) is to be evaluated at $k = \Omega_0(v|\mu|)^{-1}$, corresponding to the condition for resonant pitch angle scattering. The parallel diffusion coefficient is given by (Earl 1974)

$$\kappa = \frac{v^2}{4}\int_0^1 \frac{(1-\mu^2)^2 d\mu}{D_{\mu\mu}}\,. \tag{5}$$

For particle energies where power for resonant scattering lies at wavenumbers for which $kz_c \gg 1$ (i.e., nonrelativistic proton energies in Fig. 2), the spectrum given by equation (C1) reduces to

$$P(k) = Az_c(\delta B)^2(kz_c)^{-\delta}\,, \tag{6}$$

where $A = 2\delta \sin(\pi/\delta)$ and $\delta B = (\tilde{\sigma}^2)^{1/2}$ is the rms value of the wave field. Using equations (4) and (6) in equation (5) and setting $\delta = 5/3$ and $z_c = 10^5$ cm, one obtains, for protons,

$$\kappa(p) = \kappa(p_0)(p/p_0)^{4/3}\,, \tag{7}$$

where

$$\kappa(p_0) = 2.4 \times 10^{12}(\delta B/B_0)^{-2}\ \mathrm{cm^2\ s^{-1}}\,, \tag{8}$$

and $p_0 = mv_0$ is the momentum at the injection energy $E_0 = 100$ keV. Setting $U_2 = U_1/r$, $\kappa_2 = f^{-1}\kappa_1$ (note that $B_{01} = B_{02} = B_0$ for $\theta_1 = 0°$) and letting $\Delta p/\Delta t \rightarrow dp/dt$, equation (3) integrates to (for nonrelativistic energies)

$$(E/E_0)_{max} = (1 + \nu t)^{3/2}\,, \tag{9}$$

where

$$\nu = \frac{4(r-1)}{9r(1+r/f)}\frac{U_1^2}{\kappa_1(p_0)}\,. \tag{10}$$

From Table 1, $U_1 = 3.3 \times 10^8$ cm s^{-1} and $r = 3.85$. Using $(\delta B/B_0)_1^2 = 0.2$ and $(\delta B/B_0)_2^2 = 0.4$ ($f = 2$), $\nu \approx 10^3$ s^{-1}. For $t = 6.6 \times 10^{-3}$ s, $\nu t \approx 6.6$, and, from equation (9), $(E/E_0)_{max} \approx 21$, which is consistent with results for $\theta_1 = 0°$ in Figure 7. This close correspondence between the simulation results and predictions based upon application of both quasi-linear theory and diffusive shock acceleration theory is rather good, despite the turbulence level and injection energy used in the simulation. Specifically, the turbulence level is relatively high (i.e., $\delta B \approx B_0$), in which case diffusion coefficients derived using quasi-linear theory are suspect. Also injection energies are relatively small (i.e., $U_1/v_0 \approx 1$), in which case diffusive shock acceleration theory is not strictly applicable, since terms of order $(U_1/v)^2$ are neglected when matching upstream and downstream solutions at the shock. This latter point may explain why the spectrum for $\theta_1 = 0°$ (and other angles as well) folds over at lower energies, and assumes a monotonically decreasing form only when $E/E_0 \gtrsim 5$ (i.e., when $[U_1/v]^2 \lesssim 0.1$ and diffuse acceleration theory is applicable). In any case, the agreement between the predicted and simulated values of $(E/E_0)_{max}$ for a parallel shock is evidence that simulated energy spectrum is evolving with time as expected from theory.

Inversion of equation (9) yields an estimate of time required to reach a nonrelativistic energy $(E/E_0)_{max} \gg 1$ at a parallel shock; that is, $\nu t \approx (E/E_0)_{max}^{2/3}$. Using $(E/E_0)_{max} \approx 10^3$ (corresponding to the maximum energy reached within 6.6×10^{-3} s at $\theta_1 = 75°$ in Fig. 7), $\nu t \approx 10^2$ or $t \approx 10^{-1}$ s, which, although ~ 15 times longer than the simulation run, is still well within 1 s.

To estimate expected scattering length scales we note that since $\kappa = \lambda v/3$, the upstream parallel mean free path λ_1 is, using equations (7) and (8),

$$\lambda_1(p) = \lambda_1(p_0)(p/p_0)^{1/3} , \quad (11)$$

where

$$\lambda_1(p_0) = 1.6 \times 10^4 (\delta B/B_0)_1^{-2} \text{ cm} . \quad (12)$$

In units of the injection gyroradius $\rho_{01} = 915$ cm, equation (11) can be written in terms of kinetic energy as

$$\lambda_1(E)/\rho_{01} \approx 18(\delta B/B_0)_1^{-2}(E/E_0)^{1/6} , \quad (13)$$

revealing a weak dependence on energy. For $(\delta B/B_0)_1^2 = 0.2$, $\lambda_1(E_0)/\rho_{01} \approx 90$, and $\lambda_1(100E_0)/\rho_{01} \approx 200$. Scattering scale lengths on the order of these estimates are consistent with those typically seen upstream in trajectory plots such as Figures 5 and 6.

c) *Energy Spectra*

We now compare the simulated energy spectra (Fig. 8) with those derived from existing theoretical models. Two aspects of the spectra in Figure 8 stand out. First, as emphasized earlier, after a fixed acceleration time cutoff ($500\tau_{01}$), the upper energy attained increases with increasing θ_1. Second, beyond an energy that increases slightly with θ_1 (i.e., $E/E_0 \approx 5$ and ≈ 10 for $\theta_1 = 0°$ and 75°), each spectrum decreases monotonically with energy, with the narrow, exponential-like spectra evolving to broader, power law–like spectra as θ_1 increases. It is reasonable to conclude that in the quasi-parallel regime, the increase of spectral slope with energy is simply a consequence of the relatively short cutoff time. If this is indeed the case, and if one extrapolates the quasi-parallel spectra at lower energies to higher energies, then, at least within a limited energy range (i.e., $E/E_0 \approx 10$–100), all the spectra show remarkably similar forms (except the 0° spectrum, which has not evolved sufficiently and is therefore too narrow). This similarity suggests that above a certain energy, the steady state spectrum is independent of how the relative contributions from the first-order Fermi and shock drift acceleration processes depend on θ_1. Rather, it is the common element of spatial diffusion and the resultant statistical distribution in the number of shock encounters that determine the spectrum. This is consistent with predictions from diffusive shock acceleration theory.

The effects of drift acceleration at oblique shocks have been incorporated into the diffusive shock acceleration formalism (e.g., Toptyghin 1980; Jokipii 1982; Drury 1983). The most revealing approach is that of Jokipii (1982), who explicitly retained gradient and curvature drifts in the transport equation. For the simple case of a planar shock with geometry shown in Figure 1, Jokipii (1982) obtained a steady state energy spectrum (in the shock frame) of the form

$$\frac{dj(E)}{dE} \propto [E(E + 2m_0 c^2)]^{-\Gamma} \delta[Y - Y_0 - \eta(E - E_0)] \quad (14)$$

for a source continuously injected at $X = 0$, $Y = Y_0$ with energy E_0, where

$$\Gamma = \frac{r + 2}{2(r - 1)} \quad (15)$$

is the spectral slope, $r = U_{X1}/U_{X2}$ is the compression ratio, and

$$\eta = \frac{c(B_{Z1}/B_1^2 - B_{Z2}/B_2^2)}{q(U_{X1} - U_{X2})}$$
$$= (q\epsilon_Y)^{-1} \frac{(\xi r - 1)(r \sin^2 \theta_1)[(\xi r + 1) \sin^2 \theta_1 - 1]}{(r - 1)[\cos^2 \theta_1 + (\xi r)^2 \sin^2 \theta_1]}$$
$$= (q\epsilon_Y)^{-1} F(r, \theta_1) , \quad (16)$$

where $\epsilon_Y = U_{X1}B_{Z1}/c = U_{X2}B_{Z2}/c$ is the mean electric field magnitude (in the shock frame), $B_{X2} = B_{X1}$, $B_{Z2} = \xi r B_{Z1}$, and $\xi = (M_{A1}^2 - \cos^2 \theta_1)/(M_{A1}^2 - r \cos^2 \theta_1)$ have been used (note that Jokipii 1982 assumes $\xi = 1$, which is valid when $M_{A1}^2 \gg r \cos^2 \theta_1$). For the nonrelativistic energies appropriate here, equation (14) becomes

$$\frac{dj(E)}{dE} \propto E^{-\Gamma} \delta[Y - Y_0 - \eta(E - E_0)], \quad E \ll m_0 c^2 . \quad (17)$$

The important results are that the spectral exponent is independent of θ_1, and a given energy E is associated with a unique Y through the δ-function. As emphasized by Jokipii (1982), drift can limit the maximum energy gain if the shock is limited in the Y or "updrift" direction.

The spectral exponent Γ is given for each θ_1 in Table 1. The variation in r with θ_1 results from the relatively small Alfvén Mach number ($M_{A1} = 3$) and plasma beta ($\beta_1 = 0.14$) used. At larger M_{A1}, r, and therefore Γ, are relatively insensitive to θ_1. For $\theta_1 < 45°$, there are too few points to allow a reliable extrapolation of Γ to higher energies. For $\theta_1 \geq 45°$, fits to the spectra in Figure 8 over the limited energy ranges where Γ is nearly constant yield $\Gamma(45°) = 1.35(8 \lesssim E/E_0 \lesssim 50)$, $\Gamma(60°) = 1.68(13 \lesssim E/E_0 \lesssim 130)$, and $\Gamma(75°) = 1.86$ $(13 \lesssim E/E_0 \lesssim 130)$. The corresponding theoretical estimates are 1.25, 1.32, and 1.36. The simulated spectra are consistently steeper than the theoretical values (percentage differences are 8%, 27%, and 37% for 45°, 60°, and 75°, respectively), although, considering the differences between the two approaches as well as errors involved in estimating a steady state Γ for the spectra in Figure 8, the agreement is rather good.

One reason why the simulated Γ may be larger than theory predicts is that, at least for 45° and 60°, the spectra are really still evolving for $E/E_0 \gtrsim 10$ (Fig. 7); however, at 75°, where the simulated spectrum is essentially steady state and one would expect the best agreement between theory and simulation, the agreement is actually the worst. Perhaps of more significance are the facts that diffusive theory cannot include statistical fluctuations in θ_1, and more importantly, diffusive theory assumes that particle distributions remain isotropic right up to the shock. This latter assumption probably breaks down at 75°, where energy gains come predominantly from drift, and, therefore, anisotropies near the shock are expected to be large. These points, however, are beyond the scope of the present paper and are subjects for further work. However, based upon estimates derived by extrapolating the simulated energy spectra, we conclude that the simulations predict spectra that are in reasonable agreement with solutions from steady state diffusion theory. We emphasize that in the time-dependent regime the simulations predict that as θ_1 increases, the spectra form with increasing rapidity. More quantitative comparisons can be made when time-dependent solutions to the diffusion equation including drifts are available.

The δ-function in equation (14) gives, as a function of θ_1, the relative energy gained through the drift (ΔE_D) and first-order Fermi (ΔE_F) processes. Since $\Delta E = E - E_0 = \Delta E_D + \Delta E_F$ is the total energy gain, $\Delta E_D = q\epsilon_Y \Delta Y$, and $\Delta Y = Y - Y_0 = \eta \Delta E$, then

$$\Delta E_D/\Delta E = F(r, \theta_1) . \quad (18)$$

Using the results in Table 1 to evaluate F, we obtain for $\Delta E_D/\Delta E(\theta_1)$: 0 (0°), −0.08 (15°), 0.06 (30°), 0.34 (45°), 0.66 (60°), and 0.91 (75°). (The negative values result when $\sin \theta_1 < [\xi r + 1]^{-1/2}$ in eq. (16), indicating angles where curvature drift, which drives particles antiparallel to ϵ_Y, exceeds the gradient drift, which drives particles parallel to ϵ_Y; Jokipii 1982). The remarkable feature implied by the solution in equation (14) is that Γ is independent of θ_1 even though the contribution from the drift acceleration varies from 0% at 0° to over 90% at 75°. The simulations are consistent with these predictions, at least in a qualitative sense. More quantitative comparisons will be necessary to verify equation (18), particularly at intermediate θ_1.

d) *Implications for Prompt Acceleration of Protons during Solar Flares*

In situations where severe time constraints are absent and energy loss processes are negligible, questions concerning the acceleration rate may be of secondary importance. However, during solar flares, which are inherently dynamic processes, observations (e.g., of X-ray and gamma-ray emissions) provide time constraints that must be met by acceleration models. The simulation results discussed earlier showed prompt ion acceleration to 50 MeV or more can occur within a small fraction of a second. Here we consider the effects upon ion acceleration of Coulomb collisional losses and shocks which, although rapidly formed, are relatively short-lived.

Collisional losses can play an important role during particle acceleration in solar flares. Since the rate at which particles lose energy in a fully ionized plasma depends upon the particle energy as well as the density and temperature of the ambient plasma, the criterion that the acceleration rate exceed the collisional loss rate places severe constraints on the location of the acceleration site in the solar corona. The implications of this point were discussed by Achterberg and Norman (1980) in relation to diffuse acceleration at parallel shocks. The well-known expressions for the energy loss of protons due to Coulomb collisions in a fully ionized plasma (e.g., Trubnikov 1965; Achterberg and Norman 1980) can be written as

$$\left(\frac{dE}{dt}\right)_C = \begin{cases} -E/\tau_{pe} & E_{\rm th} < E < E_m \\ 4/3\sqrt{\pi}(E/E_m)^{-3/2}(E/\tau_{pe}) & E > E_m \end{cases}, \quad (19)$$

where

$$\tau_{pe} = (2\nu_{pe})^{-1} = \frac{3}{8\sqrt{2\pi}} \left(\frac{m_p}{m_e}\right)^{1/2} \frac{m_p^{1/2}(k_{\rm B} T_e)^{3/2}}{\lambda_{pe} e^4 n_e}, \quad (20)$$

where ν_{pe} is the proton-electron collision frequency,

$$\lambda_{pe} = \ln \left[\frac{3}{2e^3} \left(\frac{k_{\rm B}^3 T_e^3}{\pi n_e} \right)^{1/2} \right]$$

is the Coulomb logarithm, $E_{\rm th} = 3k_{\rm B} T_e/2$, and $E_m = (m_p/m_e)E_{\rm th}$. Coulomb loss rates increase linearly with proton energy $E < E_m$, maximize at $E \approx E_m$, and then decrease as $E^{-1/2}$ for $E > E_m$. Collisional losses can be safely neglected if the bulk of the protons are accelerated from $E = E_0 > E_{\rm th}$ to $E > E_m$ in a time $T_a \ll \tau_{pe}$. The e-folding loss time τ_{pe} is plotted in Figure 11 versus electron density n_e for different electron temperatures T_e. The values $n_e = 10^{10}$ cm^{-3} and $T_e = 10^7$ K assumed for the simulation yields $E_m = 1.6$ MeV and $\tau_{pe} = 36$ s; thus, our neglect of collisional losses for all θ_1 was justified (e.g., Fig. 7). (Note that relative to the plasma upstream, that downstream of the shock is both compressed [$n_{2e} > n_{1e}$] and heated [$T_{2e} > T_{1e}$], so τ_{pe} is generally different on either side of the shock).

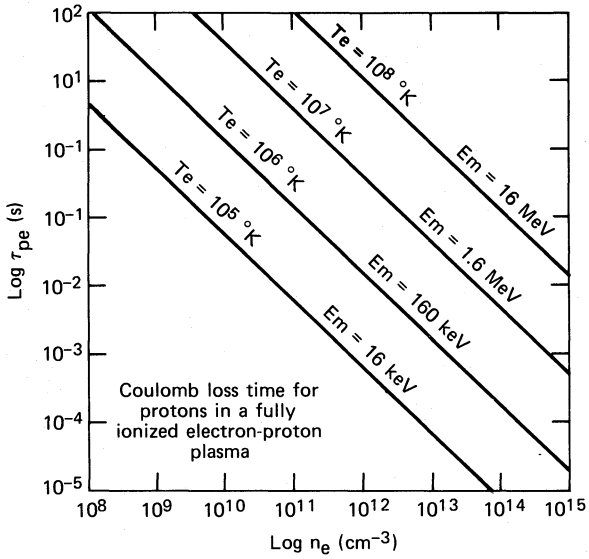

FIG. 11.—Coulomb loss time (eq. [20]) for protons in a fully ionized electron-proton plasma vs. electron density. Each curve corresponds to a different electron temperature T_e. The quantity $E_m = (m_p/m_e)(3k_{\rm B} T_e/2)$ is the proton energy at a velocity equal to the electron thermal velocity.

Using Figures 7 and 11, we can estimate the maximum n_e (for $T_e = 10^7$ K) for each θ_1. An extrapolation of the results for $\theta_1 = 0°$ in Figure 7 indicates that the bulk of the particle population will exceed ~1.5 MeV beyond $T_a \approx 3000\tau_{01} \approx 4 \times 10^{-2}$ s, which implies that losses at 0° are negligible (i.e., $T_a/\tau_{pe} \lesssim 0.1$) as long as $n_e \lesssim 10^{12}$ cm^{-3}. For $\theta_1 = 75°$, $T_a \lesssim 80\tau_{01} \approx 10^{-3}$ s, which implies that losses are negligible in this case as long as $n_e \lesssim 10^{13}$–10^{14} cm^{13}; for the superfast component, $T_a \lesssim 8\tau_{01} \approx 10^{-4}$ s, which implies $n_e \lesssim 10^{14}$–10^{15} cm^{-3}. Thus, acceleration can proceed at electron densities ~100 or more times larger when the shock is nearly perpendicular than when it is parallel. Therefore, when the shock is quasi-perpendicular, proton acceleration can take place lower in the solar atmosphere, where the energetic protons are closer to the target material with which they collide and generate, among other things, the characteristic neutral radiation (gamma rays and neutrons). Of course, the above estimates assume T_e is constant, which is not the case on the Sun, where T_e generally decreases as n_e increases with increasing depth in the solar atmosphere. For example, when $T_e < 4.2 \times 10^5$ K, $E_m < 100$ keV, and collisional losses for injection at 100 keV are less severe for any θ_1. Also, since the acceleration rate scales as $(\delta B/B_0)^2$ for a given θ_1, a decrease in this quantity by a factor of 100 yields a corresponding decrease in the maximum n_e estimated above.

Finally, we note that based upon GRS data, Chupp (1984) posed the question: "Is it possible to find a single, primary,

repetitive acceleration mechanism operative in a flare, or will only a fast, cyclic, multistage process meet observational constraints for both electrons and ions?" The work reported by Papadopoulos *et al.* (1985) on the formation time ($\sim$ few microseconds) of oblique shocks and the results shown in the present paper suggest that the combined stages of shock formation and proton acceleration from 100 keV to greater than 50 MeV can occur within a time interval as short as 10 ms. If several such shocks, separated in time by several seconds, were to form and decay within ~ 1 s, then as far as existing experiments are concerned, the accelerator would appear as a single repetitive mechanism. This scenario is a possible explanation for multiple events produced in the GRS data during solar flares, with the onset of each event being nearly simultaneous (to within less than 1 s) over the range of photon energies from 40 keV to ~ 50 MeV (Chupp 1984).

V. SUMMARY AND CONCLUSIONS

In this paper we have addressed the problem of charged particle acceleration at oblique, fast-mode, collisionless MHD shock waves. Our specific goal was to study how the acceleration rate depends upon the angle θ_1 between the shock normal and mean upstream magnetic field when magnetic irregularities exist on either side of the shock. To treat the general situation where θ_1, the level of magneitc turbulence ($\delta B/B_0$), the shock strength (or compression ratio) r, and the energy of injected particles can assume a range of values, we have performed test particle simulations. The particle code, which is fully relativistic in particle energy, integrates the particle equation of motion to obtain particle phase-space orbits in a system that consists of the shock plus magnetostatic turbulence (in the plasma rest frame) upstream and downstream of the shock. Particles are accelerated through a combination of the shock drift process, which dominates at quasi-perpendicular ($45° \lesssim \theta_1 \leq 90°$) shocks, and the first-order Fermi process, which dominates at quasi-parallel ($0° \leq \theta_1 \lesssim 45°$) shocks.

The advantages of this straightforward (but time-consuming) approach over that which involves solving the cosmic-ray transport equation (including drifts) across the shock are as follows: (1) particles can be injected at velocities v_0 for which $U_1 \sec \theta_1/v_0 \gtrsim 1$ (U_1 = shock speed), in which case the large energy gains and anisotropies produced by drift acceleration violate the diffusion approximation in the shock vicinity; (2) the gyrophase and pitch angle dependence of the drift process is properly handled; (3) large-amplitude fluctuations ($\delta B \approx B_0$) are easily incorporated, and the resulting nonlinear wave-particle interactions are properly treated; (4) the time-dependent development of particle distributions (e.g., energy spectra) can be studied as a function of the important parameters (i.e., $U_1 \sec \theta_1/v_0$, r, $\delta B/B_0$). The details of the model were described in § II and the appendices.

As an illustrative application of the numerical code, we studied the case of proton acceleration at shocks in the lower solar corona to simulate prompt ion acceleration during solar flares. For reasonable numerical values of the relevant physical parameters (Table 1), we injected an ensemble of 100 keV protons at the shock and examined the resultant distribution (~ 2100 particles) after 500 gyroperiods (6.6 ms in a 50 G upstream magnetic field). Only θ_1 was varied for each run. The numerical results were described in § III, and specific aspects of these results were discussed in detail in § IV. Notable results are summarized below.

1. For $\theta_1 = 75°$, $\sim 1\%$ of the protons were accelerated to energies greater than 50 MeV in fewer than 7 ms, which is a period well below the resolution of relevant instruments (e.g., 2 s for the GRS on *SMM*).

2. The percentage of protons accelerated beyond 10 MeV within 7 ms increase with increasing θ_1, from 0% at 0°, to a maximum of 9% at 60°.

3. In the quasi-perpendicular regime, a separate population extending from 100 keV to ~ 10 MeV was produced in a superfast phase lasting only ~ 10 gyroperiods (~ 100 μs).

4. The peak energy attained at the parallel shock (~ 2–3 MeV within 7 ms) agreed well with that expected from diffusive shock acceleration theory.

5. At $\theta_1 = 75°$, the simulated energy spectrum below 10 MeV did not evolve further beyond 7 ms. Between 1 and 10 MeV, the slope of the simulated spectrum is 1.9, while that expected from steady state diffusion theory is 1.4. We suggest that this discrepancy (35%) may be attributable to the breakdown near the shock of the quasi-isotropic assumption implicit in the theory. Further simulation work along this line is clearly necessary.

6. The increase in acceleration rate as θ_1 increases implies that, when Coulomb collisional losses are considered, acceleration can proceed at electron densities ~ 100 times larger when the shock is nearly perpendicular than when it is parallel. This implies that acceleration at quasi-perpendicular shocks can occur lower in the solar atmosphere, when the energetic protons are closer to target material with which the protons collide and generate, among other things, gamma-ray and neutron emission.

7. The combined stages of shock formation and proton acceleration to ≥ 50 MeV can occur within a time interval as short as 10 ms at quasi-perpendicular shocks. If several such shocks, separated in time by several seconds, were to form and decay within ~ 1 s, then as far as existing instruments are concerned, the accelerator would appear as a single repetitive mechanism.

Note that if the variance of the magnetic field fluctuations were reduced by a factor as large as 100, so that upstream $(\delta B_1/B_{01})^2 = 0.2$ would go to 0.002, acceleration rates would be correspondingly decreased. Thus, the spectrum at $\theta_1 = 75°$ would be formed within 0.7 s, still well within observational constraints. Also, when the escape boundaries are set closer to the shock, or the amplitude of the random field is damped away from the shock, or both, the energy spectra in the quasi-perpendicular regime in Figure 7 would depart from power-law forms and would exhibit more exponential-like forms, with spectral slopes increasing with increasing energy.

We conclude that the exact orbit, test-particle simulations can provide important insight into the process of time-dependent acceleration at turbulent, oblique shocks, and can reveal microstructure (e.g., the superfast acceleration phase in the quasi-perpendicular range) not accessible to diffusion theory. By their nature, however, simulations of this sort are limited, for practical reasons, to at most a few thousand gyroperiods per particle. To obtain solutions at longer times, or in the limit, in the steady state, Monte Carlo simulations or use of the cosmic-ray transport equation are clearly the most practical approaches, provided the physical effects implied by the simulations are incorporated in some manner.

This work was supported in part by the JHU/APL Independent Research Development Program under US Navy contract N00024-83-C-5301, in part by NSF grant ATM 83-05537, and in part by NASA grant NSG-7055.

APPENDIX A

DETAILS OF THE INTEGRATION SCHEME

Here we summarize the relations used to transform among the frames K_1, K_2, and K and discuss the numerical procedure used to integrate equations (1) and (2). We allow particle motion to be relativistic but restrict the relative velocities among the reference frames to be nonrelativistic. Relative to frame K, the system K_i ($i = 1$–2) moves at velocity

$$\boldsymbol{U}_i = (U_i \cos \delta_i,\ 0,\ U_i \sin \delta_i)\ , \tag{A1}$$

and the axis z_i of K_i lies among the unperturbed field

$$\boldsymbol{B}_{0i} = (B_{0i} \cos \theta_i,\ 0,\ B_{0i} \sin \theta_i) \tag{A2}$$

(see Fig. 1). Particle orbits are obtained by integrating equations (1) and (2) of § II in frame K_i. At injection ($t = 0$) for each particle, the origins of the three frames coincide. Let $[\boldsymbol{x}_i(t), \boldsymbol{p}_i(t)]$ be a particle's phase point relative to K_i in $(\boldsymbol{x}, \boldsymbol{p})$ space at time t, where $\boldsymbol{x}_i = (x_i, y_i, z_i)$, $\boldsymbol{p}_i = (p_{ix}, p_{iy}, p_{iz})$. Then, given $[\boldsymbol{x}_1(t), \boldsymbol{p}_1(t)]$ in K_1, $[\boldsymbol{x}_2(t), \boldsymbol{p}_2(t)]$ relative to K_2 is given by

$$\boldsymbol{x}_2(t) = R\boldsymbol{x}_1(t) + \boldsymbol{A}_1 t\ , \tag{A3a}$$

and

$$\boldsymbol{p}_2(t) = R\boldsymbol{p}_1(t) + \gamma_1 \boldsymbol{A}_1\ , \tag{A3b}$$

where $\gamma_i = [1 + (p_i/m_0 c)^2]^{1/2}$ and R is a rotation matrix given by

$$R = \begin{bmatrix} \cos \Delta & 0 & \sin \Delta \\ 0 & 1 & 0 \\ -\sin \Delta & 0 & \cos \Delta \end{bmatrix}, \tag{A4}$$

where $\Delta = \theta_2 - \theta_1$, and $\boldsymbol{A}_1$ is the constant vector

$$\boldsymbol{A}_1 = \begin{bmatrix} U_1 \sin (\theta_2 - \delta_1) - U_2 \sin (\theta_2 - \delta_2) \\ 0 \\ U_1 \cos (\theta_2 - \delta_1) - U_2 \cos (\theta_2 - \delta_2) \end{bmatrix}. \tag{A5}$$

The inverse transformation from K_2 to K_1 is

$$\boldsymbol{x}_1(t) = R^T \boldsymbol{x}_2(t) - \boldsymbol{A}_2 t\ , \tag{A6a}$$

and

$$\boldsymbol{p}_1(t) = R^T \boldsymbol{p}_2(t) - \gamma_2 \boldsymbol{A}_2\ , \tag{A6b}$$

where R^T is the transpose of R, and $\boldsymbol{A}_2 = R^T \boldsymbol{A}$, is the constant vector

$$\boldsymbol{A}_2 = \begin{bmatrix} U_1 \sin (\theta_1 - \delta_1) - U_2 \sin (\theta_1 - \delta_2) \\ 0 \\ U_1 \cos (\theta_1 - \delta_1) - U_2 \cos (\theta_1 - \delta_2) \end{bmatrix}. \tag{A7}$$

The transformation from K_i to K is

$$\boldsymbol{X}(t) = S_i \boldsymbol{x}_i(t) + \boldsymbol{U}_i t\ , \tag{A8a}$$

and

$$\boldsymbol{P}(t) = S_i \boldsymbol{p}_i(t) + \gamma_i \boldsymbol{U}_i\ , \tag{A8b}$$

where

$$S_i = \begin{bmatrix} \sin \theta_i & 0 & \cos \theta_i \\ 0 & 1 & 0 \\ -\cos \theta_i & 0 & \sin \theta_i \end{bmatrix},$$

and $\boldsymbol{X} = (X, Y, Z)$, $\boldsymbol{P} = (P_X, P_Y, P_Z)$. To obtain the above relations terms of order $(U_i/c)^2$ were neglected.

Equations (1) and (2) of § II were solved for each particle for given realizations of $\boldsymbol{b}(z)$ (see Appendix B) in the upstream and downstream regions using the following algorithm. At $t = 0$ a particle is injected at $[\boldsymbol{x}_i(0), \boldsymbol{p}_i(0)]$ in frame K_i. The particle is integrated along its orbit using Hamming's modified predictor-corrector scheme (e.g., Carnahan, Luther, and Wilkes 1969) with an initial time step $h_t^{(0)} = 10^{-a}\tau_{0i}$ (where $\tau_{0i} = 2\pi/\Omega_{0i}$, $\Omega_{0i} = qB_{0i}/m_0 c$) and an upper truncation error bound ϵ_t. Values used for typical runs were $a = 2$, $\epsilon_t = 10^{-4}$. The integration scheme automatically halves $h_t^{(0)}$ up to 10 times until local truncation errors are less than ϵ_t. Shock crossings are detected by testing the equation

$$X(t) = x_i(t) \sin \theta_i + z_i(t) \cos \theta_i + U_i t \cos \delta_i \tag{A10}$$

at each time step for a sign change. For example, suppose that during the interval $h_t^{(0)}$ between times t_j and $t_{j+1}^{(0)} = t_j + h_t^{(0)}$ the

particle makes its kth shock crossing, say from upstream to downstream, so that $i = 1$ in equation (A10). Then $X(t_j) < 0$, while $X(t_{j+1}^{(0)}) > 0$. If t_{kc} denotes the actual crossing time ($t_j < t_{kc} < t_{j+1}^{(0)}$), then successively more accurate estimates of t_{kc} are obtained by halving $h_i^{(0)}$, restarting the integration at t_j, and iterating n times until a criterion $t_{j+1}^{(n)} - t_j = h_i^{(n)} \leq \epsilon_c$ is satisfied, at which point we set $t_{kc} = t_{j+1}^{(n)}$. For a typical value of $\epsilon_c = 10^{-5}$, $n = 3$–5. At this point, $[\boldsymbol{x}_1(t_{kc}), \boldsymbol{p}_1(t_{kc})]$ and t_{kc} are used in equation (A3) to obtain $[\boldsymbol{x}_2(t_{kc}), \boldsymbol{p}_2(t_{kc})]$, which provide the new initial conditions for orbit integration in K_2. Tracing a particle orbit in the wave-shock system actually consists of several initial value calculations using, equations (1) and (2), with the initial conditions for each integration obtained from the transformations (A3) and (A6).

Particles are permitted to escape the wave-shock system by passing through predefined escape boundaries at

$$X_i^e = \Lambda_i |\cos \theta_i| \qquad (i = 1 \text{ or } 2) , \tag{A11}$$

for a given escape length $\Lambda \geq 0$ along the mean magnetic field. Escape upstream occurs when $X < -X_1^e \leq 0$, and escape downstream occurs when $X > X_2^e \geq 0$.

APPENDIX B

GENERATION OF RANDOM FIELD REALIZATIONS

Here we give the details of how spatial realizations of the random field $\boldsymbol{b}(z) = \hat{\boldsymbol{x}} b_x(z) + \hat{\boldsymbol{y}} b_y(z)$ are generated for use in the simulation. Let $\{b(z)\}$ be a zero-mean, homogeneous random process, such that $\{b(z)\}$ denotes the ensemble of real-valued functions $b(z)$ [where $b(z) = b_x(z)$ or $b_y(z)$] of the spatial variable z, $-\infty < z < \infty$. Let $b(z)$ be a particular sample record or realization of $\{b(z)\}$ that consists of N points evenly spaced a distance h_b apart on the finite interval $[0, L]$. Let

$$N = 2^p , \tag{B1}$$

where p is a positive integer ≥ 0, and define

$$b_n = b(z = z_n = nh_b) , \qquad 0 \leq n \leq N - 1 , \tag{B2}$$

as the value of $b(z)$ at each of the N discrete points. Then the grid spacing is

$$h_b = L/(N - 1) = \tilde{L}/N , \tag{B3}$$

where $\tilde{L} = L + h_b$. For convenience in applying periodic boundary conditions to the realization along z, we define the additional point $b_N = b_0$ in equation (B2), so that there are now $N + 1$ points on $[0, \tilde{L}]$. We relate h_b to the correlation length z_c of the random field by

$$h_b = z_c/2^q , \tag{B4}$$

where q is a postive integer, $0 \leq q \leq p$. Given p, q, and z_c, the length $\tilde{L}$ is given by

$$\tilde{L} = Nh_b = 2^{p-q} z_c . \tag{B5}$$

so that there are $2^{p-q} \geq 1$ correlation lengths per interval $\tilde{L}$, with 2^q grid points per z_c. [In rough terms, two values of $\boldsymbol{b}(z)$ separated by $z = z_c$ will, on average, be completely different in magnitude, direction, or both].

The technique of synthesizing a realization of $b(z)$ is most easily understood by first considering how one would obtain the finite Fourier transform of the N points of $b(z)$ on the interval $[0, L]$. We follow here the discussion of Owens (1978). One has

$$a_m = \sum_{n=0}^{N-1} b_n e^{-ik_m z_n}, \qquad m = 0, 1, 2, \ldots, N - 1 , \tag{B6}$$

where

$$k_m = 2\pi m/(Nh_b) = 2\pi m/\tilde{L} \tag{B7}$$

is the wavenumber corresponding to wavelength $\lambda_m = \tilde{L}/m$ and is associated with the Fourier coefficient a_m. The inverse transform is

$$b_n = \frac{1}{N} \sum_{m=0}^{N-1} a_m e^{ik_m z_n} , \qquad n = 1, 2, 3, \ldots, N - 1 . \tag{B8}$$

For real b_n, only half of the a_m are unique, with

$$a_{N-m} = a_m^* , \qquad m = 1, 2, 3, \ldots, N/2 - 1 , \tag{B9}$$

where the asterisk (*) denotes complex conjugate, a_0 and $a_{N/2}$ are real, and $a_0 = 0$, so that $b(z)$ has zero mean. The largest (Nyquist) wavenumber (i.e., smallest wavelength) definable for grid spacing h_b is

$$k_L = k_{N/2} = \pi/h_b = \pi 2^q/z_c , \tag{B10}$$

while the smallest wavenumber (i.e., largest wavelength) is

$$k_S = k_1 = 2\pi/\tilde{L} = 2^{-p+1} k_L . \tag{B11}$$

Thus, $k_L/k_S = 2^{p-1}$.

An estimate of the one-sided (i.e., $0 \leq k < \infty$) wavenumber power spectrum $P(k)$ at k_m is (Bendat and Piersol 1971)

$$P_m = \left(\frac{2h_b}{N}\right) |a_m|^2 . \tag{B12}$$

Only the modulus $|a_m|$ of each a_m is recoverable from equation (B12). Thus, the a_m are not uniquely defined for use in equation (B8). Following Owens's (1978) suggestion, we generate the phase angles ϕ_m randomly from a distribution uniform over the interval $(0, 2\pi)$ and use $|a_m| = (NP_m/2h_b)^{1/2} = N(P_m/2\tilde{L})^{1/2}$ to obtain

$$a_m = |a_m| e^{i\phi_m} = N(P_m/2\tilde{L})^{1/2} e^{i\phi_m} . \tag{B13}$$

Upon taking the complex conjugate of equations (B8) and (B13), and requiring the b_n to be real, one obtains

$$b_n = \sum_{n=0}^{N-1} A_m e^{-ik_m z_n} , \tag{B14}$$

where

$$A_m = (P_m/2\tilde{L})^{1/2} e^{i\phi_m} . \tag{B15}$$

Note equation (B14) is in exactly the same form as equation (B6). Thus, fast Fourier transform (FFT) techniques routinely used to Fourier analyze real input data b_n by generating the a_m via equation (B6) can also be used to synthesize a particular realization of the b_n from the coefficients A_m in equation (B15) once P_m and the random ϕ_m are given. The A_m also satisfy

$$A_{N-m} = A_m^* , \qquad m = 1, 2, 3, \ldots, N/2 - 1 , \tag{B16}$$

where again we set $A_0 = 0$. Thus, each set of random ϕ_m, $m = 1, 2, 3, \ldots, N/2 - 1$, generates one particular realization of b_z on $[0, L]$.

As pointed out by Owens (1978), it is possible to generate two field realizations with one use of the FFT on equation (B14) by defining A_m by

$$\bar{A}_m = (P_m/2\tilde{L})^{1/2}(e^{i\phi_m} + e^{i\phi_m'}) , \tag{B17}$$

and using $\bar{A}_m$ in equation (B14) to generate the N element complex vector $\bar{b}_n$, such that Re $(\bar{b}_n)$ and Im $(\bar{b}_n)$ each constitute a realization of $b(z)$. When ϕ_m and ϕ_m' are independent random phases, the two resultant realizations are statistically independent of each other. The form (B17) also allows one to conveniently generate the x and y components of the random field $\boldsymbol{b}(z) = \hat{\boldsymbol{x}} b_x(z) + \hat{\boldsymbol{y}} b_y(z)$ by specifying the polarization of each Fourier component. If we set $\phi_m' = \phi_m + s_m \pi/2 (s_m = +1 \text{ or } -1)$, $P_m \rightarrow P_m/2$, then $b_x(z) =$ Re $(\bar{b}_n)$ and $b_y(z) =$ Im $(\bar{b}_n)$ are the components of the two-dimensional random field $\boldsymbol{b}(z)$ formed by superposing circularly polarized Fourier components. When $s_m = +1(-1)$, the (nonpropagating) mth plane wave component would appear to have positive (negative) helicity to an observer moving along the z-axis toward positive or negative z in the plasma frame. The sign s_m can be predefined for all m or randomly generated for each m.

It remains to discuss how the synthesized random field $b(z)$ [$b_x(z)$ or $b_y(z)$] is used in equation (1) of § II. Once generated using the FFT, the $N + 1$ discrete values b_n of $b(z)$ (i.e., the N values b_n, $n = 0, 1, 2, \ldots, N - 1$, plus the value $b_N = b_0$) reside in the $N + 1$ element vector $\{F(j)\}$, $j = 1, 2, 3, \ldots, N + 1$. For convenience, we translate the origin via $z \rightarrow z - \tilde{L}/2$ so that the center of the realization lies at the origin of frames K_1 or K_2, and label field points by the index $l = n - N/2$, so that now $z_l = lh_b$, $l = -N/2, (-N + 1)/2, \ldots, -1, 0, 1, \ldots, (N - 1)/2, N/2$. Then, $b(z_l) = b_l = F(j = l + 1 + N/2)$. A given point $z = \xi$ will generally not coincide with a field point, and ξ may also lie outside the interval $[-\tilde{L}/2, \tilde{L}/2]$ containing the field points b_l. In the former case, we use linear interpolation between field points, and in the latter case we impose periodic boundary conditions along z as follows. For ξ within $(-\infty, \infty)$ but ξ outside $[-\tilde{L}/2, \tilde{L}/2]$, we calculate the appropriate index l for ξ using $l = \text{INT}[z/h_b + N/2] - N/2$, where $z = \xi - \text{INT}[\xi/\tilde{L} + \text{SGN}(\xi)0.5]$ now lies in the interval $[-\tilde{L}/2, \tilde{L}/2]$ (where INT $\equiv$ integer, SGN $\equiv$ sign). Index l labels the field point $F(j), j = l + 1 + N/2$, that is the nearest field point to the left of z, and linear interpolation is used to find $b(\xi)$ via

$$b(\xi) = b(z) = F(j) + [F(j + 1) - F(j)][z/h_b - l] . \tag{B18}$$

This equation provides the field point $b_x(z)$, $b_y(z)$, or both at each point along a particle's orbit.

It is of interest to model the case where the amplitude of the transverse MHD wave field decreases with increasing distance from the shock, so that scattering is more efficient closer to the shock. Such is the case, for example, upstream of the Earth's bow shock (e.g., Hoppe *et al.* 1971) and some interplanetary shocks (Tsurutani, Smith, and Jones 1983), where the field of MHD waves is apparently generated by low-energy ions streaming away from the shock. Such waves are ultimately convected back to and through the shock by the super-Alfvénic upstream bulk flow. We include the possibility for spatial dependence of wave amplitudes by the following simple model. First, we assume that in the first approximation the MHD waves are nonpropagating in the plasma frame. Let D be the distance from the shock along $\boldsymbol{B}_0$ over which the amplitude of the wave field decreases to, say, one-half its value at the shock, and assume $D \gg z_c$ so that the random wave field remains at least quasi-homogeneous. Given the particle's position $\boldsymbol{x}_i(t)$ in plasma frame K_i, we obtain its coordinate $X = X(x_i, z_i, t)$ in shock frame K using equation (A10), and let $\boldsymbol{b}_i(z_i) \rightarrow \Gamma_i(X)\boldsymbol{b}_i(z_i)$, where $\Gamma_i(X)$ is a "damping" function. We have assumed the simple form

$$\Gamma_i(X) = [1 + |X|/X_i^d]^{-1} , \tag{B19}$$

where

$$X_i^d = D_i|\cos\theta_i| \qquad (i = 1 \text{ or } 2)\,, \tag{B20}$$

so that $\Gamma_i(X_i^d) = \Gamma_i(0)/2$.

APPENDIX C

POWER SPECTRUM

We obtain the amplitudes of the Fourier coefficients in equations (B15) or (B17) by assuming a one-sided ($0 \le k < \infty$) wavenumber power spectral density $P(k)$ of the general form

$$P(k) = \frac{2\delta \sin(\pi/\delta) z_c \tilde{\sigma}^2}{1 + (kz_c)^\delta}\,, \qquad 1 < \delta < \infty\,, \tag{C1}$$

where z_c is the correlation length of the random field and $\tilde{\sigma}^2$ is the variance. The power spectrum $P(k)$ of the random field $b(z)$ [$b_x(z)$ or $b_y(z)$] is related to the autocorrelation function

$$R(\xi) = \lim_{L\to\infty} \frac{1}{L}\int_0^L b(z)b(z+\xi)dz \tag{C2}$$

by the Fourier cosine transform pair (e.g., Rice 1954)

$$P(k) = 4\int_0^\infty R(\xi)\cos(k\xi)d\xi\,, \tag{C3}$$

and

$$R(\xi) = \frac{1}{2\pi}\int_0^\infty P(k)\cos(k\xi)dk\,, \tag{C4}$$

then

$$R(0) = \lim_{L\to\infty}\frac{1}{L}\int_0^L b^2(z)dz = \psi^2\,, \tag{C5}$$

where ψ^2 is the mean square value of $b(z)$. If $b(z)$ is a random function of z with zero mean, then the variance $\tilde{\sigma}^2 = \psi^2$, and by equations (C4) and (C5),

$$\int_0^\infty P(k)dk = 2\pi R(0) = 2\pi\tilde{\sigma}^2\,, \tag{C6}$$

which is satisfied by equation (C1). The form (C1) with $\delta \approx 1$–2 is characteristic of the spectra of Alfvénic fluctuation in the interplanetary medium (Matthaeus and Goldstein 1982), and is suggested by Owens (1978) to be a reasonable form for synthesizing magnetic field realizations for numerical studies of cosmic-ray transport (Owens considered the case $\delta = 3/2$). The special case $\delta = 2$ yields the familiar exponential autocorrelation function $R(\xi) = R(0)e^{-\xi/z_c}$ used by Kaiser (1974) to generate magnetic fluctuations to study energetic particle propagation in magnetostatic fluctuations. Brinca (1984) extended Owens's (1978) method and generated realizations of time-dependent electric and magnetic random fields using the form (C1) with $\delta = 3/2$–3 to study ion transport in the Earth's magnetosheath.

For given values of δ, z_c, and $\tilde{\sigma}^2$, equation (C1) is evaluated at each discrete k_m in equation (B7), and $P_m = P(k_m)$ is substituted into equation (B15) or (B17). Whereas the synthesized realization $b(z)$ on $[0, L]$ is composed of Fourier components with wavenumbers k within $[k_S, k_L]$ (eqs. [B10] and [B11]), the normalization (C2) assumes $0 \le k < \infty$. Therefore the variance σ^2 determined by a statistical analysis of the N points b_n, $n = 1, 2, 3, \ldots, N-1$, yields

$$\sigma^2 = \frac{1}{N}\sum_{n=1} b_n^2 < \tilde{\sigma}^2\,. \tag{C7}$$

Normally, for $\delta \approx 1$–2 and $k_S \ll z_c^{-1} \ll k_L$, $\tilde{\sigma}^2$ exceeds σ^2 by less than 10%. However, σ^2 is the relevant physical quantity and is therefore quoted in the text.

REFERENCES

Achterberg, A., and Norman, C. A. 1980, *Astr. Ap.*, **89**, 353.
Armstrong, T. P., Pesses, M. E., and Decker, R. B. 1985, in *Collisionless Shocks in the Heliosphere: Reviews of Current Research*, ed. B. T. Tsurutani and R. G. Stone (*Geophys. Monog. Ser.*, **35**, 271).
Axford, W. I. 1981, *Proc. 17th Internat. Cosmic Ray Conf.* (Paris), **12**, 155.
Axford, W. I., Leer, E., and Skadron, G. 1978, *Proc. 15th Internat. Cosmic Ray Conf.* (Plovdiv), **11**, 132.
Bai, T., Hudson, H. S., Pelling, R. M., Lin, R. P., Schwartz, R. A., and Von Rosenvinge, T. T. 1983, *Ap. J.*, **267**, 433.
Barbosa, D. D. 1979, *Ap. J.*, **233**, 383.

Bell, A. R. 1978, *M.N.R.A.S.*, **182**, 147.
Bendat, J. S., and Piersol, A. G. 1971, *Random Data: Analysis and Measurement Procedures* (New York: Interscience).
Blandford, R. D., and Ostriker, J. P. 1978, *Ap. J.* (*Letters*), **221**, L29.
Brinca, A. L. 1984, *J. Geophys. Res.*, **89**, 115.
Carnahan, B., Luther, H. A., and Wilkes, J. O. 1969, *Applied Numerical Methods* (New York: Wiley).
Christon, S. P. 1982, *J. Geophys. Res.*, **86**, 8852.
Chupp, E. 1984, *Ann. Rev. Astr. Ap.*, **22**, 359.
Decker, R. B. 1983, *J. Geophys. Res.*, **88**, 9959.
Decker, R. B., and Vlahos, L. 1985*a*, *J. Geophys. Res.*, **90**, 47.
———. 1985*b*, *Proc. 19th Internat. Cosmic Ray Conf.* (La Jolla), **4**, 10.
Drury, L. O'C. 1983, *Rept. Progr. Phys.*, **46**, 973.
Earl, J. A. 1974, *Ap. J.*, **193**, 231.
Ellison, D. C. 1981, Ph.D. thesis, Catholic University of America.
Ellison, D. C., and Ramaty, R. 1985, *Ap. J.*, **298**, 400.
Forman, M. A., and Webb, G. M. 1985, in *Collisionless Shocks in the Heliosphere: Reviews of Current Research*, ed. B. T. Tsurutani and R. G. Stone (*Geophys. Monog. Ser.* **34**, 91).
Frost, K. J., and Dennis, B. R. 1970, *Ap. J.*, **165**, 655.
Gary, S. P. 1985, *Ap. J.*, **288**, 342.
Gary, S. P., Gosling, J. T., and Forslund, D. W. 1981, *J. Geophys. Res.*, **86**, 6691.
Gosling, J. T., Asbridge, J. R., Bame, S. J., and Feldman, W. C. 1979, in *Particle Acceleration Mechanisms in Astrophysics*, ed. J. Arons, C. Max, and C. McKee, (*AIP Conf. Proc. No. 56*), p. 81.
Greenstadt, E. W., and Fredericks, R. W. 1979, in *Solar System Plasma Physics*, Vol. **3**, ed. C. F. Kennel, L. J. Lanzerotti, and E. N. Parker (Amsterdam: North-Holland), p. 3.
Helfer, H. L. 1952, *Ap. J.*, **117**, 177.
Hoppe, M. M., Russell, C. T., Frank, L. A., Eastman, T. E., and Greenstadt, E. W. 1981, *J. Geophys. Res.* **86**, 4471.
Jokipii, J. R. 1971, *Res. Geophys. Space Phys.*, **9**, 27.
———. 1982, *Ap. J.*, **255**, 716.
Jokipii, J. R., and Morfill, G. E. 1985, *Proc. 19th Internat. Cosmic Ray Conf.* (La Jolla), **3**, 132.
Kaiser, T. B. 1974, Ph.D. thesis, University of Maryland.
Kennel, C. F., *et al.* 1984, *J. Geophys. Res.*, **84**, 5419.
Krymskii, G. F. 1977, *Dokl. Akad. Nauk. SSSR*, **234**, 1306.
Kulsrud, R. 1979, in *Particle Acceleration Mechanisms in Astrophysics*, ed. J. Arons, C. Max, and C. McKee, (*AIP Conf. Proc. No. 56*), p. 13.
Lampe, M., and Papadopoulos, K. 1977, *Ap. J.*, **212**, 886.
Lee, M. A. 1982, *J. Geophys. Res.*, **87**, 5063.
———. 1983, *J. Geophys. Res.*, **88**, 6109.
Lee, M. A., and Fisk, L. A. 1982, *Space Sci. Rev.*, **32**, 205.
Legage, P. O., and Cesarsky, C. J. 1983, *Astr. Ap.*, **125**, 249.
Leroy, M. M., Winske, D., Goodrich, C. C., Wu, C. S., and Papadopoulos, K. 1982, *J. Geophys. Res.*, **87**, 5081.
Matthaeus, W. H., and Goldstein, M. L. 1982, *J. Geophys. Res.*, **87**, 6011.
Melrose, D. B. 1983, *Solar Phys.*, **89**, 149.
Owens, A. J. 1978, *J. Geophys. Res.*, **83**, 1673.
Papadopoulos, K., Goodrich, C. C., Cargill, P., and Vlahos, L. 1985, *Eos Trans. Am. Geophys. Union*, **66**, 331.
Pyle, K. R., Simpson, J. A., Barnes, A., and Mihalov, J. D. 1984, *Ap. J.* (*Letters*), **282**, L107.
Ramaty, R. 1979, in *Particle Acceleration Mechanism in Astrophysics*, ed. J. Arons, C. Max, and C. McKee (*AIP. Conf. Proc. No. 56*), p. 135.
Ramaty, R., *et al.* 1980, in *Solar Flares*, ed. P. Sturrock (Boulder: Colorado Associated Press), p. 117.
Rice, S. O. 1954, in *Selected Papers on Noise and Stochastic Processes*, ed. N. Wax (New York: Dover), p. 133.
Sarris, E. T., and Krimigis, S. M. 1985, *Ap. J.*, **298**, 676.
Sarris, E. T., and Van Allen, J. A. 1974, *J. Geophys. Res.*, **79**, 4157.
Scholar, M., Ipavich, F. M., Gloeckler, G., and Hovestadt, D. 1983, *J. Geophys. Res.*, **88**, 1977.
Sentman, D. D., Kennel, C. F., and Frank, L.A. 1981, *J. Geophys. Res.*, **86**, 4365.
Smith, D. F., and Brecht, S. H. 1985, *J. Geophys. Res.*, **90**, 205.
Sturrock, P. A. 1980, in *Solar Flares*, ed. P. A. Sturrock (Boulder: Colorado Associated Press), p. 411.
Tanaka, M., and Papadopoulos, K. 1983, *Phys. Fluids*, **26**, 1697.
Toptyghin, I. N. 1980, *Space Sci. Rev.*, **26**, 157.
Trubnikou, B. A. 1965, in *Rev. Plasma Phys.*, Vol. **1**, ed. M. A. Leontovich (New York: Consultants Bureau), p. 105.
Tsurutani, B. T., and Lin, R. P. 1985, *J. Geophys. Res.*, **90**, 1.
Tsurutani, B. T., Smith, E. J., and Jones, D. E. 1983, *J. Geophys. Res.*, **88**, 5045.
Van Nes, P., Reinhard, R., Sanderson, T. R., Wentzel, K.-P., and Zwickl, R. D., 1984, *J. Geophys. Res.*, **89**, 2122.
Vlahos, L., *et al.* in *Proc. Solar Maximum Mission Workshop, Energetic Phenomena on the Sun*, ed. M. R. Kundu and B. Woodgate, in press.
Webb, G. M., Axford, W. I., and Teresawa, T. 1983, *Ap. J.*, **270**, 537.
Wentzel, D. G. 1974, *Ann. Rev. Astr. Ap.*, **12**, 71.
Winske, D., and Leroy, M. M. 1984, *J. Geophys. Res.*, **89**, 2673.

ROBERT B. DECKER: Johns Hopkins University, Applied Physics Laboratory, Laurel, MD 20707

LOUKAS VLAHOS: Department of Physics, University of Thessaloniki, Thessaloniki, Greece GR-54006